

1 **IITM High-Resolution Global Forecast Model Version 1: An attempt**  
2 **to resolve monsoon prediction deadlock**

3 R. Phani Murali Krishna<sup>1</sup>, Siddharth Kumar<sup>1</sup>, A. Gopinathan Prajeesh<sup>2</sup>, Peter Bechtold<sup>3</sup>, Nils Wedi<sup>3</sup>,  
4 Kumar Roy<sup>4</sup>, Malay Ganai<sup>1</sup>, B. Revanth Reddy<sup>1</sup>, Snehlata Tirkey<sup>1</sup>, Tanmoy Goswami<sup>1</sup>-, Radhika  
5 Kanase<sup>1</sup>, -Sahadat Sarkar<sup>1</sup>-, Medha Deshpande<sup>1</sup>-, Parthasarathi Mukhopadhyay<sup>1,5</sup>  
6

7 <sup>1</sup>Indian Institute of Tropical Meteorology, Ministry of Earth Sciences, Dr. Homi Bhabha Road, Pune 411008, India

8 <sup>2</sup> King Abdullah University of Science and Technology, Saudi Arabia

9 <sup>3</sup> ECMWF

10 <sup>4</sup> University of Victoria, Canada

11 <sup>5</sup> Department of Earth and Environmental Sciences, Indian Institute of Science Education and Research, Berhampur 760003,  
12 Odisha, India  
13

14

15

16 *Correspondence to:* Dr. P. Mukhopadhyay (mpartha@tropmet.res.in; [parthasarathi64@gmail.com](mailto:parthasarathi64@gmail.com))

17

18

19

20

21

22

23

24

25

26

27

28 **Abstract.** The prediction of Indian monsoon rainfall variability, affecting a country with a population of billions, remained  
29 one of the major challenges of the numerical weather prediction community. While in recent years, there has been a  
30 significant improvement in predicting the synoptic scale transients associated with the monsoon circulation, the intricacies of  
31 rainfall variability remained a challenge. Here, an attempt is made to develop a global model using a dynamic core of a cubic  
32 octahedral grid that provides a higher resolution of 6.5 km over the global tropics. This high-resolution model has been  
33 developed to resolve the monsoon convection. Reforecasts with the IITM High-resolution Global Forecast Model (HGFM)  
34 have been run daily from June through September 2022. The HGFM model has a wave-number truncation of 1534 in the  
35 cubic octahedral grid. The monsoon events have been predicted with a ten-day lead time. The HGFM model is compared to  
36 the operational GFS T1534. While the HGFM provides skills comparable to the GFS, it shows better skills for higher  
37 precipitation thresholds. This model is currently being run in experimental mode and will be made operational.

38

39

40

41

42

43

44

45

46

47

48

49

50

51

52

53

54

56 In spite of significant improvement in numerical weather prediction skills in the last decades (Bechtold et al., 2008;  
57 Magnusson and Kallen, 2013; Hoffman et al., 2018), predictions of tropical rainfall variability remain a challenge (Westra et  
58 al., 2014; Prakash et al., 2016). Stephens et al. (2010) demonstrated that the models predict ~~in the tropics too many rainy~~  
59 ~~days too many rainy days in the tropics~~, which are in the lighter rain category. The challenges of tropical rainfall variability  
60 have also been demonstrated by Watson et al., 2017. The vagaries of the Indian monsoon every year affect the lifestyle of  
61 billions of people and the economy of the Indian sub-continent ~~modulating, modulating~~ its Gross Domestic Product (GDP)  
62 (Gadgil and Gadgil, 2006). It is, therefore, of the utmost importance to improve the weather prediction skill in general and  
63 extreme precipitation events in particular. With the increase ~~of in~~ computing power, the resolution of numerical weather  
64 prediction models ~~have has~~ been increasing, and global models with a resolution of 1~7 km have become a reality (Majewski  
65 et al., 2002; Satoh et al., 2005; Miura et al., 2007; Staniforth and Thuburn, 2012; Li et al., 2015; Satoh et al., 2019; Wedi et  
66 al., 2020). The higher resolution of Numerical Weather Prediction (NWP) models has been found to produce a realistic  
67 rainfall variability across scales including diurnal variation, better Madden Julian Oscillation (MJO) variability and seasonal  
68 mean climate (Kinter et al., 2013; Rajendran and Kitoh, 2008; Skamarock et al., 2012; Molod et al., 2015; Crueger et al.,  
69 2018; Giorgetta et al., 2018). In India, operational NWP was initiated with a moderate resolution of T80 and then gradually  
70 enhanced to T382, T574 (Prasad et al., 2011, 2014, 2017), and very recently to T1534 (Mukhopadhyay et al., 2019). The  
71 advantage of using a higher resolution (T1534~12.5 km) as against the lower resolution T574 (~27 km) was found by  
72 enhancement of the model skill by 2 days (Rao et al., 2019). The National Centre for Environmental Prediction (NCEP) GFS  
73 model with 21 members has been used for probabilistic forecasts since June 2018 (Deshpande et al., 2021). The high-  
74 resolution GFS T1534 is found to enhance the skill of heavy rainfall ~~event events~~ (Mukhopadhyay et al., 2019), tropical  
75 cyclones, and even block level prediction of rainfall (block is a sub-division of ~~a districts districts~~ in India, typically of the  
76 size of the grid of GFS T1534). However, the skill of the GFS T1534 for the prediction of extremely heavy precipitation can  
77 still be improved, particularly over the orographic regions of India, such as the southern coastal state of Kerala, India  
78 (Mukhopadhyay et al., 2021).

79 The 12-km deterministic and the ensemble model based on the GFS ~~do~~ show reasonably good skill in capturing the monsoon  
80 rainfall with 3 to 5 days lead time. The skill of the GFS forecast for the Indian monsoon has been reported by  
81 Mukhopadhyay et al. (2019), and the skill of tropical cyclones with the Global Ensemble Forecast System (GEFS) has also  
82 been reported ~~in by~~ Deshpande et al. (2021) and Kanase et al. (2023). However, in a recent study, Mukhopadhyay et al.  
83 (2021) showed that three state-of-the-art ensemble forecast systems, namely the GEFS, the United Kingdom Meteorological  
84 Office (UKMO) based NCMRWF Ensemble Prediction System (NEPS) run by National Centre for Medium Range Weather  
85 Forecasting (NCMRWF) and the Integrated Forecasting System (IFS) by ECMWF struggled to capture the extremely heavy  
86 rainfall over Kerala state of India during August 2018 and August 2019 extremely heavy rainfall episode. This, in fact,  
87 brought up the limitation of the model in resolving the rainfall variability over the Indian region and, more importantly, over

88 the orographic region. One of the limitations in resolving the regional variabilities of rainfall is the horizontal resolution  
89 which does not allow the model to resolve the smaller scale processes. Therefore, a need was felt to enhance the horizontal  
90 resolution of the existing GFS-based forecasting system. As running of a model close to the convection permitting model (at  
91 a resolution lesser than 10 km) is computationally too expensive in conventional linear reduced Gaussian grids, it was  
92 thought to build a weather model with a grid ~~whiehthat~~ has a variable resolution from the pole to the equator. In view of this,  
93 the GFS linear reduced Gaussian Grid at triangular truncation 1534 is replaced by an equivalent truncation of 1534 in a  
94 triangular cubic octahedral (Tco) grid. The equivalent model resolutions of the linear T1534 and the cubic Tco1543 grids are  
95 displayed in Fig. 1a. Indeed, as the linear grid has a roughly uniform grid point resolution of 12.5 km, the octahedral grid has  
96 a resolution of about 8 km in the Polar Regions and around 6 km in the tropical band. One of the prominent examples of the  
97 Global NWP model with the Tco grid is that of the European Centre for Medium-Range Weather Forecasts (ECMWF)  
98 model suites. The Tco grid provides several advantages (ECMWF Documentation Cy43r1, 2016) over that of the  
99 conventional reduced Gaussian linear grid (Fig. 1a), to name a few- significant reduction in computation cost, improved  
100 representation of orography, better filtering, and better conservation properties. These properties of Tco make it a better  
101 candidate, particularly for the utilization of high-performance computers (HPC).

102 ~~This paper is the first attempt to best of our knowledge, towards building a model close to a convection permitting global~~  
103 ~~weather model in India with an emphasis to~~ To the best of our knowledge, this paper is the first attempt towards building a  
104 model close to a convection permitting global weather model in India with an emphasis on Indian monsoon rainfall  
105 variability. The details of the model development and the experiments conducted have been elaborated in Sect. 2. The model  
106 results are analysed in Sect. 3, and the conclusion of the study is summarized in Sect. 4.

## 107 **2 Model, Data, and Methodology**

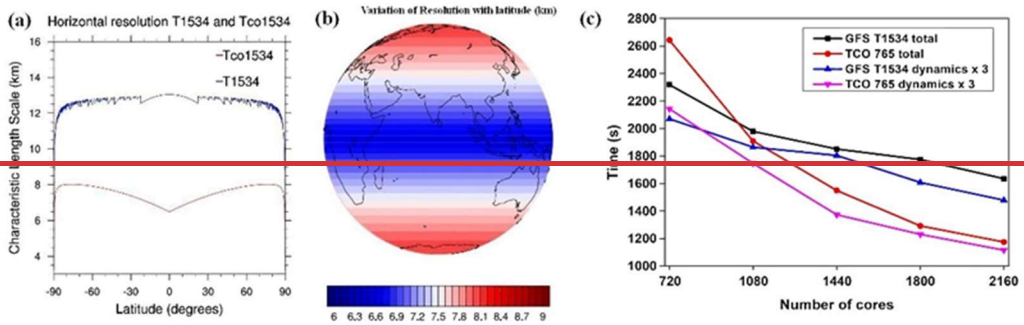
108 This new grid, namely the Triangular Cubic Octahedral (Tco) grid, has been adopted to change the existing GFS (semi-  
109 lagrangian) Gaussian linear model system. In the spectral domain, dynamical fields are represented by the sum of spherical  
110 harmonics. The total wavenumber characterizes the spherical harmonics, and the associated wavelength is the ratio of the  
111 circumference of the Earth to the total wavenumber. The value of the maximum wavenumber ( $n_{max}$ ) used to represent a  
112 field as the sum of spherical harmonics is also the spectral truncation of the model. In the case of both GFS and Tco, the  
113 value of  $n_{max}$  is 1534. For the same spectral truncation  $n_{max}$ , the number of latitude circles from the equator to the pole  
114 can vary depending on the choice of spectral transformation. For a linear grid,  $n_{max}=2N-1$ , and for a cubic grid,  $n_{max}=N-$   
115 1. Therefore, for a linear Gaussian grid, the smallest wavelength is represented by only two grid points, as is the case with  
116 the GFS 1534 model. However, in the case of triangular truncation, the smallest wavelength is represented by four grid  
117 points (in the case of the Tco grid). In triangular truncation, for the same spectral truncation, the number of latitude circles is  
118 about double that of the linear truncation. For the GFS model, the horizontal resolution is  $\sim 12.5$  km, and applying the cubic

119 grid ensures that the horizontal resolution becomes  $\sim 6.5$  km in the tropics (about half of the currently used model resolution)  
120 for the Tco grid. In the Tco grid, the number of latitude circles is 1535.

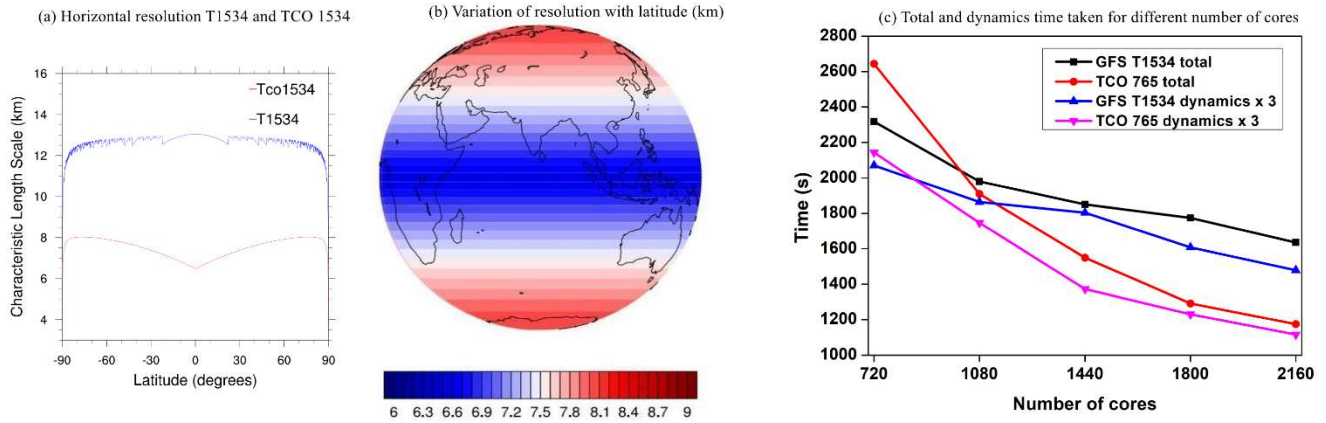
121 Once a particular choice of spectral truncation is made, the number of latitude circles becomes obvious. However, the  
122 number of longitude circles per latitude circle remains to be prescribed for ~~the creation of~~creating the global grid structure. In  
123 a fully Gaussian grid, the number of longitude circles per latitude circle remains the same throughout the latitudes from the  
124 equator to the pole. Thus, the effective resolution near the poles becomes very high compared to the equatorial regions. This  
125 specific requirement demands too many computational resources and poses ~~problems of numerical instability~~numerical  
126 ~~instability problems~~. To overcome that, in the linear Gaussian grid, the number of latitude circles decreases in a certain way  
127 from the equator toward the pole to ensure almost the same zonal resolution. For the cubic octahedral grid, the number of  
128 longitude points per latitude circle is prescribed ~~in a different way~~differently. The latitude circle closest to the pole consists  
129 of 20 longitude points, and the number of longitude points increases by 4 at each latitude circle, moving from poles towards  
130 the equator. The number of longitude points at the equator in the case of the Tco grid is given by  $N_x = 20 + 1534 * 4 = 6156$ .  
131 Therefore, the zonal grid length  $= 2\pi * R / N_x \sim 6.5$  km. In the original reduced Gaussian grid, the number of longitude points  
132 per latitude remains fixed in different blocks of latitudes. The number of latitude points jumps from one block to ~~the an~~other  
133 by a constant number. Unlike the linear reduced Gaussian grid, the horizontal resolution varies more smoothly with latitudes  
134 in Tco. The Collignon projection of a sphere obtains this configuration onto an octahedron. In the current study, the Tco grid  
135 at truncation wavenumber of 1534 is being used. This new version of the model is mentioned as HGFM (High-resolution  
136 Global Forecast Model Version 1) throughout the manuscript. Fig. 1a and Fig. 1b ~~depicts~~depict the variation of grid  
137 resolution with latitude in the GFS (SL) and HGFM (Tco).

138 Before testing the HGFM with complete physics (see Table 1 for a description of physics ~~being~~used in both versions of ~~the~~  
139 model), we have ~~developed~~made a version of HGFM with only a dynamical core following ~~the approach of~~Held and Suarez  
140 (1994), referred to as HS94. The HS94 ~~is~~was run to check the stability of the Tco grid framework. Surface boundary  
141 conditions for the Tco grid ~~were~~have been meticulously prepared to ensure the accuracy of grid-point representation.  
142 Moreover, the HGFM (Tco1534) has been developed with complete physics and incorporates essential boundary conditions,  
143 including global topography, global land-use-land-cover, etc. The HGFM at Tco1534 truncation is depicted over the globe in  
144 Fig. 1. The model has been run daily for ~~ten~~ days forecast at IITM Pratyush HPC system. To understand the computational  
145 efficiency of ~~the~~Tco model, ~~the~~time taken for one day forecast is compared for GFS 1534 and HGFM model (Tco 765 in  
146 this case) (see Fig. 1c). A comparison between GFS 1534 and Tco 765 is made because both models have ~~almost~~nearly ~~the~~  
147 same number of grid points. It is ~~evident~~clear that Tco 765 significantly saves the runtime in dynamical core and total time  
148 as well. Moreover, the Tco model is in general more scalable for higher number of cores (not shown). The model has been  
149 ~~running~~ since 2022, and here, the analyses for the summer monsoon season of June, July, August, and September (JJAS)  
150 2022 are being presented. A detailed analysis of the model run is discussed in the results section. Apart from the monsoon  
151 season (JJAS 2022), a few case studies are also discussed.

152



153



154

155 **Figure 1.** Variation of grid length with latitude in GFS (blue) and Tco (red) (a), depiction of grid resolution over the globe in Tco  
 156 grid (b), total and dynamics time taken for different number of cores (c). Time taken by GFS and HGFM for one day forecast  
 157 (Left vertical axis is total time taken and model dynamics time multiplied by 3).

158 To verify the model forecast, the daily observed gridded rainfall data from the Integrated Multi-satellite Retrievals for GPM  
 159 (IMERG) version 06B (Huffman et al., 2019) rainfall data at  $0.1^\circ \times 0.1^\circ$  (10 km) horizontal resolution is utilized for the year  
 160 of 2022 for JJAS season. Additionally, for tohe validateion of a heavy rainfall event over India, gridded rainfall data from  
 161 the India Meteorological Department (IMD) at 25 km resolution is used. The IMD rainfall data are a merged product of  
 162 gridded rain gauge observations and GPM satellite-estimated rainfall over the Indian Summer Monsoon (ISM) region (Mitra  
 163 et al., 2014). Further, the reanalysis-based parameters from the fifth generation of ECMWF atmospheric reanalyses (ERA5)  
 164 products (Hersbach and Dee, 2016) are utilized at 25 km horizontal resolution are utilized during JJAS season of the year  
 165 2022.

166 **Table 1.** Details of domain configuration and physics options used in HGFM.

Physics	Description
Radiation	Rapid Radiative Transfer Model (RRTM) for both Shortwave and Longwave (Iacono et al., 2000; Clough et al., 2005) with Monte Carlo Independent Column Approximation (McICA)

Microphysics	Formulated grid-scale condensation and precipitation (Sundqvist et al., 1989; Zhao and Carr, 1997)
Convection	Aerosol aware and Mass flux based Simplified Arakawa-Schubert (SAS) shallow convection (Pan and Wu, 1995; Han and Pan, 2011; Arakawa and Wu, 2013; Han et al., 2017)
Planetary Boundary Layer (PBL)	Hybrid Eddy-Diffusivity Mass Flux vertical turbulent mixing scheme (Han and Pan, 2011; Han et al., 2016)
Gravity Wave Drag (GWD)	Mountain blocking (Alpert et al., 1988; Kim and Arakawa, 1995; Lott and Miller, 1997) and stationary convective-forced GWD (Chun and Baik, 1998)

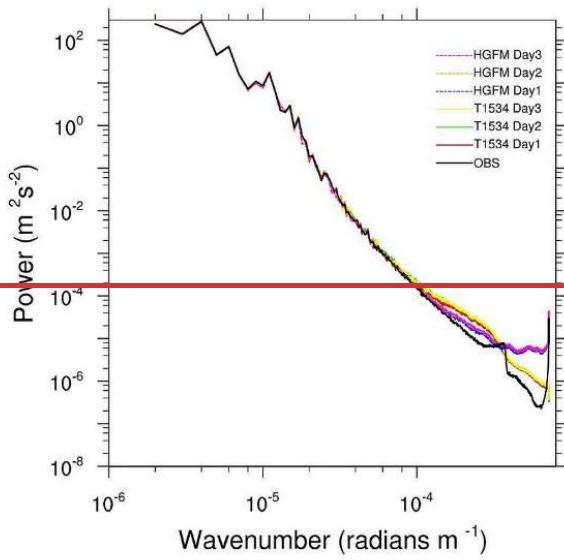
167

## 168 3 Results and Discussions

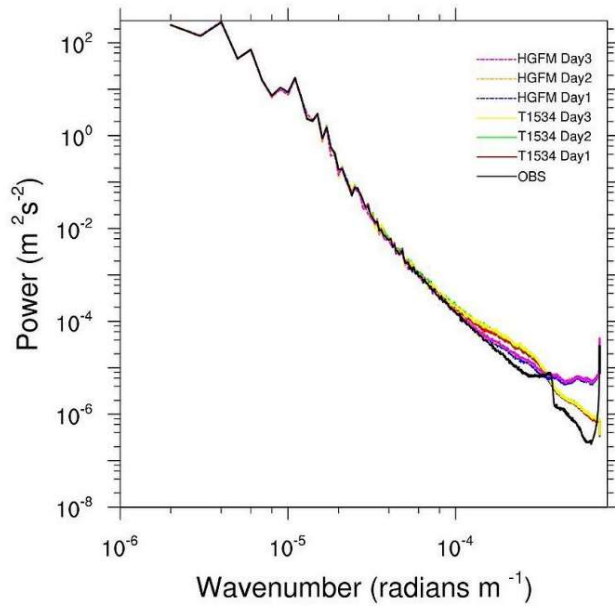
### 169 3.1 200 hPa Kinetic Energy Spectra

170 Before going into the details of model validation, the first metric to evaluate the model fidelity is to validate the Kinetic  
171 Energy (KE) spectra of 200 hPa wind. The KE spectra provide information about the distribution of kinetic energy across ~~the~~  
172 scales. A close resemblance between observed /reanalysis-based spectra and spectra produced by the model gives confidence  
173 about the accuracy of overall model configuration. The kinetic energy (KE) spectrum in the upper troposphere exhibits two  
174 clearly defined power-law patterns. From observational studies, it is established that at large-scale, rotational modes prevail  
175 ( $k^{-3}$ ), while at mesoscales, divergent modes are dominant ( $k^{-5/3}$ ) (Nastrom and Gage, 1985). Figure 2 shows the KE spectra of  
176 200 hPa wind simulated by HGFM and GFS T1534. The KE spectra for the forecast up to 3 days lead time have been  
177 compared with ERA5 data. While both the models reasonably capture  $k^{-5/3}$  behaviour of the mesoscale at the higher  
178 wavenumber, ~~but the~~ HGFM appears to capture the  $k^{-3}$  behaviour of the large scale at the lower wavenumber closer to  
179 observation. It is observed that beyond wavenumber  $10^{-4}$  there is a slight departure of the spectra from observation,  
180 especially for HGFM. However, the regions of interest in KE spectra are the  $k^{-3}$  dependence for the large scale and a less  
181 steep,  $k^{-5/3}$  dependence for the mesoscale. The tail of the spectra at higher wave-numbers typically has less energy due to the  
182 dissipation of kinetic energy with an increase of wave-number, however, models tend to dissipate the energy at higher  
183 wave-numbers at a much faster rate depending on the damping used in the model (Skamarock, 2004). To keep the spectra  
184 realistic, a common practice is to reduces the damping, which may increase the energy at higher wavenumbers, as observed  
185 in this case for HGFM. However, this will not have much impact ~~in~~ our analysis as these are the small-scale features. The  
186 KE spectra indicates that the overall configuration of both versions of the model is robust. Therefore, we now ~~we~~ turn our  
187 attention towards verification of convective available potential energy and rainfall simulations, the most desirable parameters  
188 in model forecasts.

189



190



191

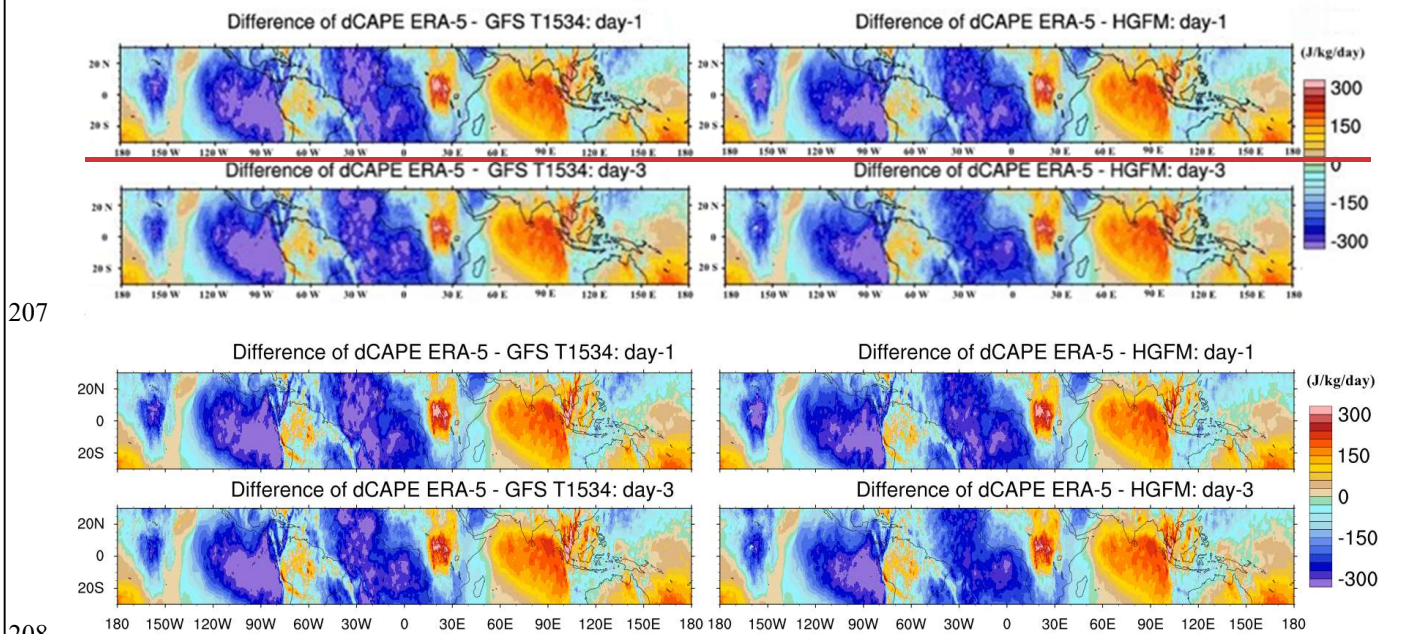
192 **Figure 2. Kinetic energy spectra of 200 hPa wind for observation and different lead times of GFS T1534 and HGFM.**

193 **3.2 Quasi-equilibrium in models**

194 Both model versions are run at high-resolutions, close to convection-permitting models' resolution. However, in this case, a  
 195 scale-aware convection scheme is used to parameterize deep convection in the model. From observational studies, it has  
 196 been established that tropical atmosphere deviates significantly from the convective-quasi equilibrium (e.g., Zhang, 2003).



197 The convective quasi-equilibrium (CQE) is the fundamental approach used in most models for parameterization of deep  
 198 convection (Arakawa and Schubert, 1974). To understand up to what the extent to which both model versions obey CQE, we  
 199 adopted the methodology suggested in by Kumar et al. (2022). The absolute value of changes in Convective Available  
 200 Potential Energy (CAPE) at daily timescales is analysed from GFS T1534 and HGFM models for the year 2022 during JJAS  
 201 and compared with the ERA-5 data (Figure not shown). Notable changes were observed in the daily dCAPE values between  
 202 GFS T1534 and HGFM compared to ERA-5. The daily dCAPE values from ERA-5 data matches-match better with the  
 203 HGFM than GFS T1534 for day 1 and day 3 lead times. The difference of dCAPE between ERA-5 and models is presented  
 204 for day-1 and day-3 lead time forecasts (Fig. 3). The dCAPE difference quantified from ERA-5 with GFS T1534 were –  
 205 49.0570 (J/kg/day) and –47.3799 (J/kg/day) for day1 and day 3 lead times, respectively. sSimilarly, with HGFM, the values  
 206 were –49.1278 (J/kg/day) and –43.7668 (J/kg/day) for day 1 and day 3 lead times, respectively.



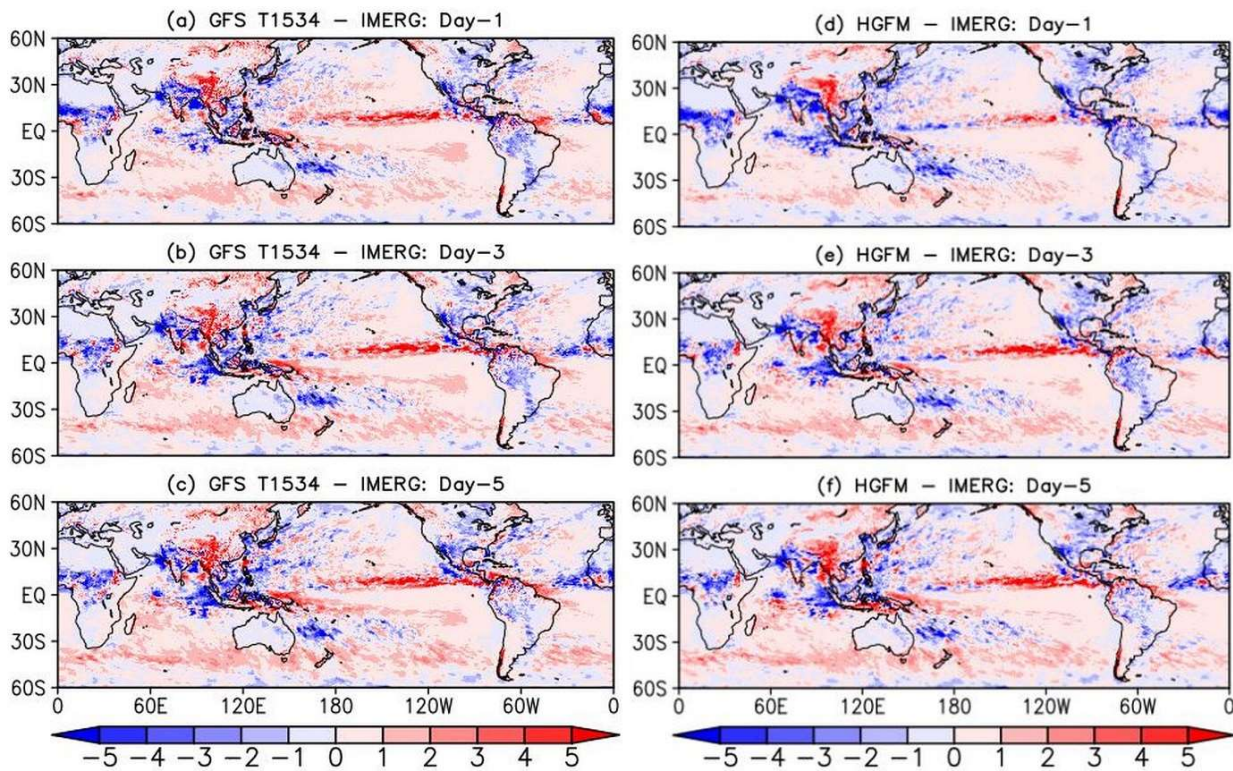
207  
 208  
 209 **Figure 3.** The difference of dCAPE from between ERA-5 and GFS T1534 for day-1 and day-3 (left panels), and  
 210 between from ERA-5 and HGFM for day-1 and day-3 (right panels).

211 **3.3 Analysis of Global pPrecipitation**

212 The global precipitation bias of GFS (left panel of Fig. 4 and HGFM (right panel) with respect to Integrated Multi-satellite  
 213 Retrievals for GPM (IMERG) data, with day 1, day 3, and day 5 lead times, is shown in Fig. 4. Both the models broadly  
 214 show a similar rainfall bias over the global land and global ocean. However, there are some subtle differences. The day 1  
 215 forecast (Fig. 4a) of GFS shows a wet bias over the equatorial eastern Pacific extending up to the tropical western Pacific.  
 216 On the other hand, the HGFM on day 1 lead (Fig. 4d) also shows a wet bias mostly confined over the tropical eastern Pacific

217 and a slight negative bias over the western Pacific. For HGFM, the positive bias of rainfall over the tropical ocean appears to  
 218 be mostly-mainly over the eastern Pacific, while that of GFS appears to ~~be over eastern Pacific and extending from the~~  
 219 eastern pacific towards the central and west Pacific for all the lead times. The eastern Pacific precipitation overestimation  
 220 could be due to improper representation of shallow convection over the region. Raymond (2017) highlighted the complex  
 221 nature of SST and associated cloudiness and convection over the region. Apart from the oceanic region, the major global  
 222 land regions (central African Continent, Maritime continent, Indian summer monsoon region, northern part of South  
 223 America) shows a negative bias in both the models at different lead times (Fig. 4) which is likely related to the model's  
 224 physical parameterizations.

225



226

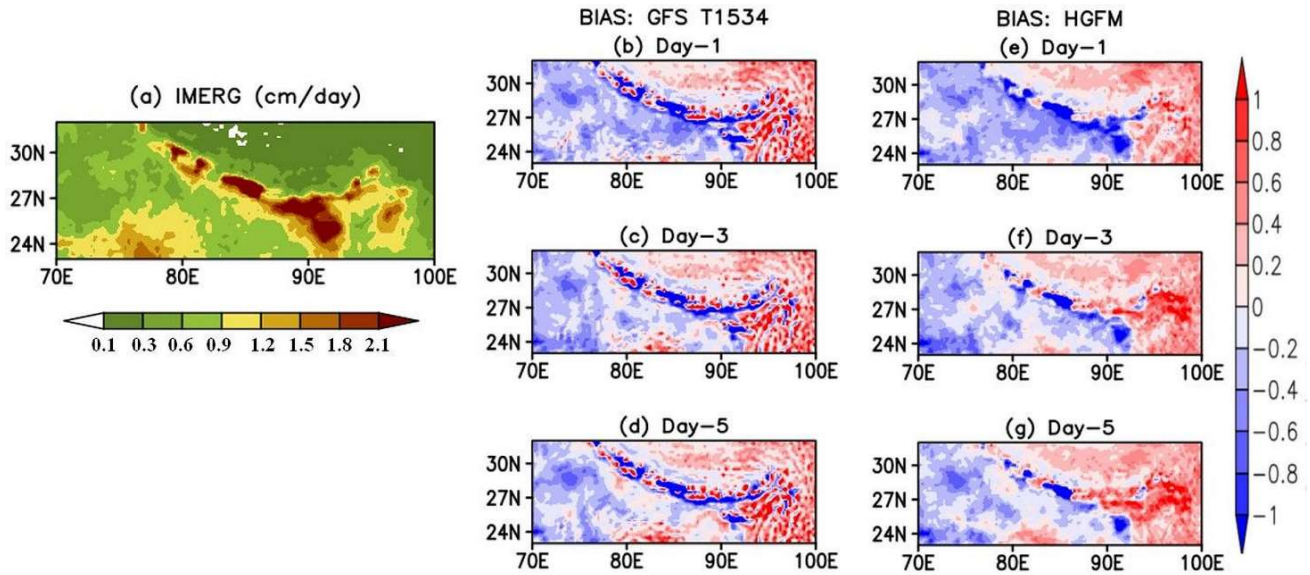
227 **Figure 4. Global JJAS precipitation bias (cm/day) of GFS T1534 (left panel) with respect to IMERG for (a) day-1, (b) day-3 and**  
 228 **(c) day-5 lead time. Right column (d-f) indicates similar plots but for HGFM.**

### 229 3.4 Indian summer monsoon precipitation and related features

230 While Fig. 4 depicted the precipitation bias over the global domain, it will be interesting to investigate the model forecast  
 231 performance over the complex orographic region over the Indian domain, the region of our utmost interest. As mentioned  
 232 earlier, one of the major advantages of using a Tco grid is ~~a-better-representation-of~~ that it better represents orography.

233 Therefore, it is imperative to investigate the forecast skill of the high-resolution HGFM model over the mountainous  
 234 Himalayan foothills, adjoining northeast India, and Western Ghats (WGs) region (shown in Fig. 5 and 6 respectively). The  
 235 GFS T1534 model forecasts indicate spurious rainfall activity over the Himalayan foothills and northeast India region for all  
 236 lead times (Fig. 5b-d). On contrary, the HGFM model with finer horizontal resolution largely resolves the spurious rainfall  
 237 over the region, as shown in Fig. 5e-g. The Gibbs waves are largely suppressed over the mountainous terrains in HGFM  
 238 compared to GFS T1534. Similarly, the precipitation distribution over the WGs region shows considerable overestimation in  
 239 GFS T1534 for all lead times (Fig. 6b-d). On the other hand, the magnitude of overestimation is decreased considerably in  
 240 HGFM forecasts, as depicted in Fig. 6e-g. Thus, the above analysis ~~highlights brings out~~ the fact that HGFM shows its  
 241 potential in predicting realistic rainfall distribution over the orographic regions.

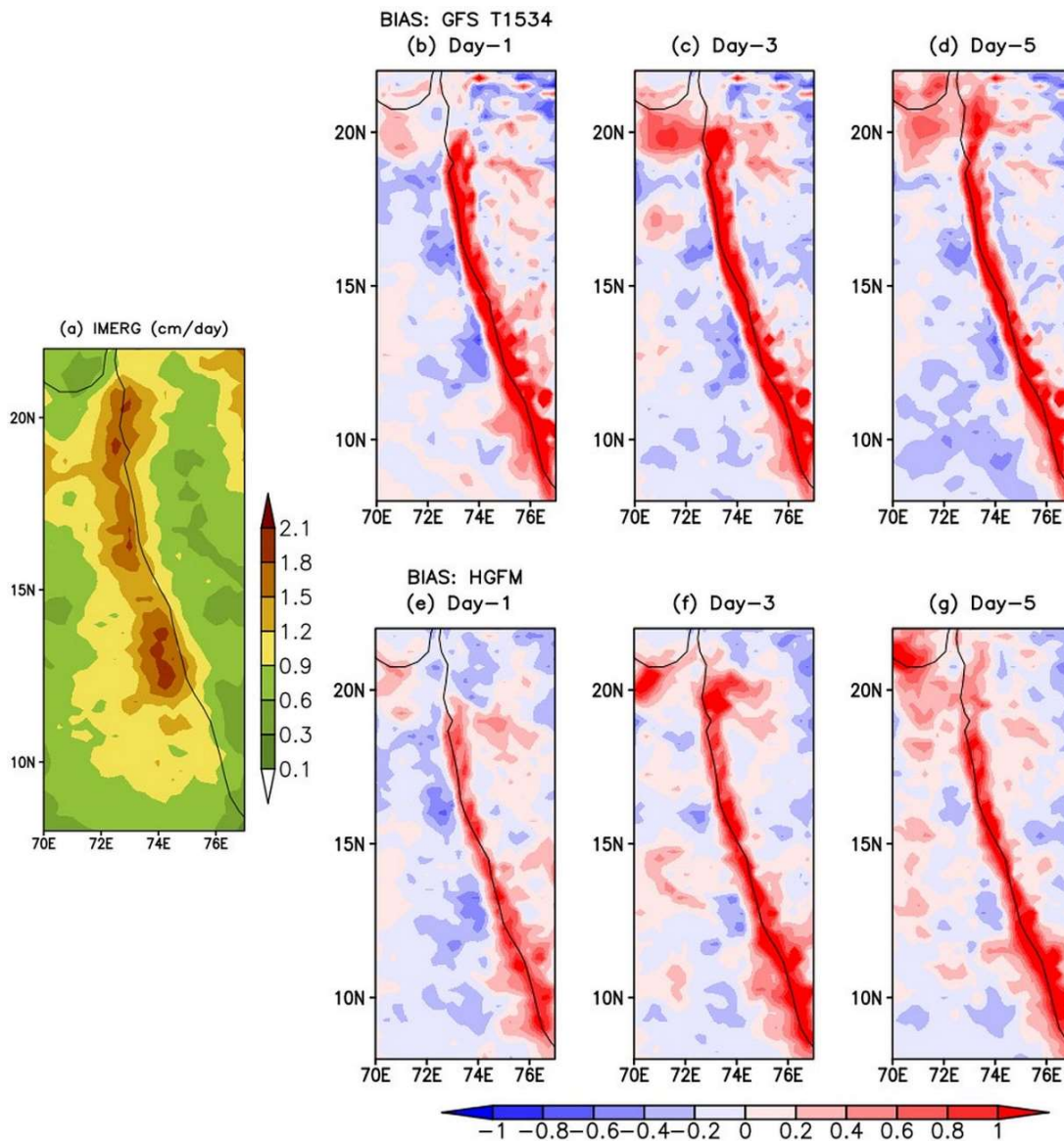
242



243

244 **Figure 5. Comparison of JJAS mean precipitation (cm/day) and Bias in IMERG data (cm/day) (a) with GFS T1534 (b, c, d) and**  
 245 **TCO 1534 (e, f, g) during 2022 over Himalayan foothills and Northeast India for day-1 day-3 and day-5 lead time.**

246



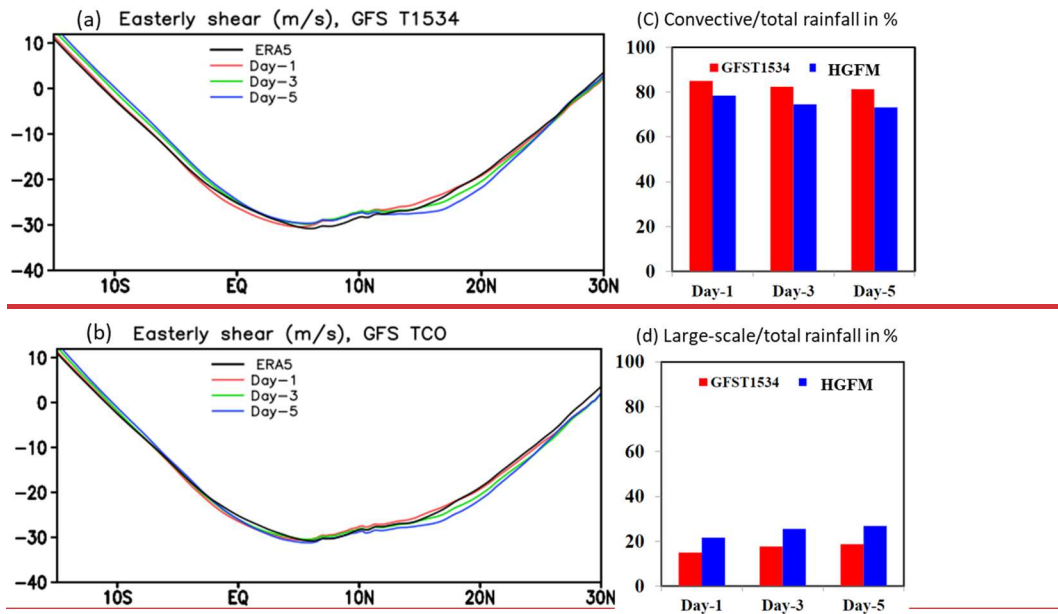
247

248 **Figure 6. Comparison of JJAS mean precipitation (cm/day) and Bias in IMERG data (cm/day) (a) with GFS T1534 (b, c, d) and**  
 249 **TCO 1534 (e, f, g) during 2022 over Western Ghats region for day-1 day-3 and day-5 lead time.**

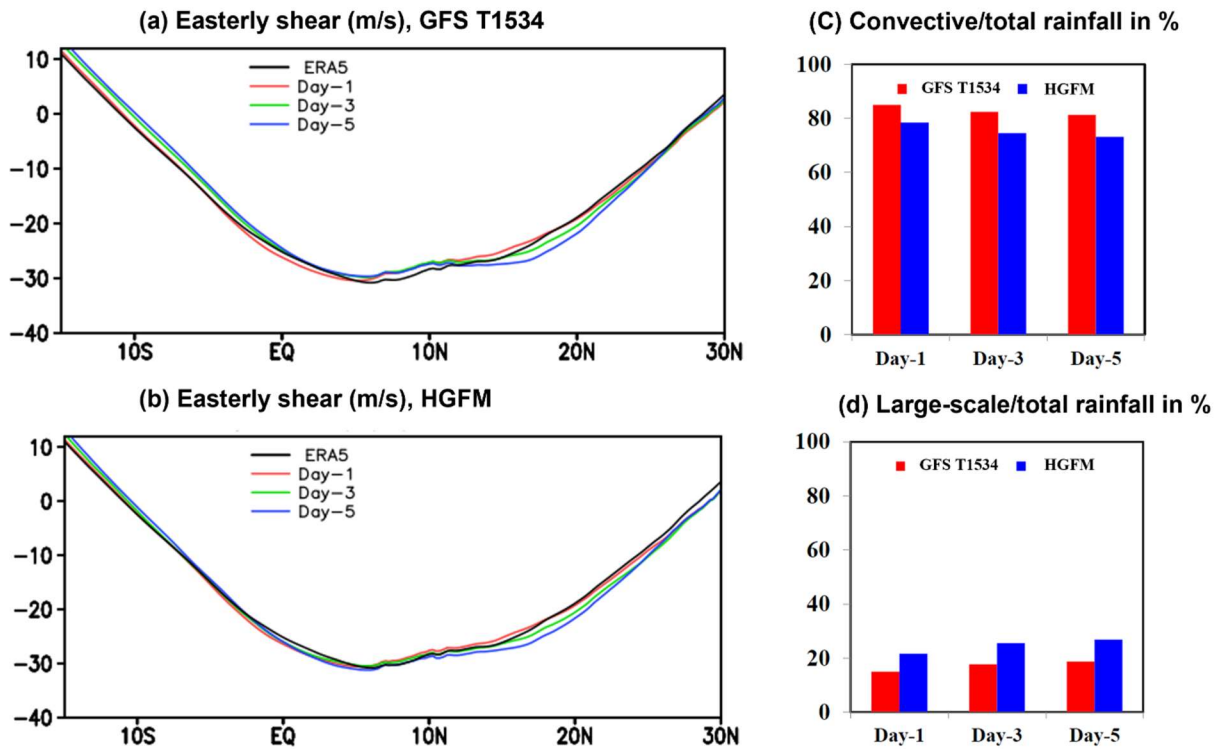
250 One of the prominent features of ISM is the vertical shear of zonal wind. Previous studies (Jiang et al., 2004; Abhik et al.,  
 251 2013) demonstrated that the vertical easterly wind shear plays a crucial role in inducing baroclinic vorticity ahead of the  
 252 northward propagation of summer intra-seasonal oscillation. ~~In order to find out~~To assess the model forecast skill in  
 253 predicting realistic easterly wind shear (difference between zonal wind at 200 and 850 hPa) during the summer monsoon  
 254 season of 2022, the vertical wind shear calculated and is represented in Fig. 7a and 7b for GFS T1534 and HGFM,  
 255 respectively, over the ISM region. Figure 7a indicates slightly weaker easterly shear in GFS T1534 compared to ERA5

256 around 10° N and 0°-15° S for all lead times. On the contrary, the HGFM ~~is able to predict~~ more realistic easterly wind shear  
 257 over ~~the~~ above regions, as shown in the Fig. 7b. It is noticeable that both models overestimate the magnitude of easterly  
 258 shear around 20° N for Day-3 and Day-5 lead times.

259 Another key feature ~~about~~ of tropical precipitation is almost equipartition of rainfall into convective and stratiform rain.  
 260 Therefore, it is important to investigate whether the relative improvement in the precipitation distribution over the ISM  
 261 region in HGFM forecasts is contributed by improved convective and large-scale precipitation. The model forecasted  
 262 convective and large-scale rainfall ratios are shown in Fig. 7c and 7d respectively. It is noteworthy that the large-scale or  
 263 stratiform rainfall plays an important role in the propagation and maintenance of the tropical intraseasonal convection,  
 264 associated with its top-heavy heating profile (Fu and Wang, 2004; Chattopadhyay et al., 2009; Deng et al., 2015). The  
 265 heating profile associated with stratiform rain also helps in large-scale organization of convection (see, for example,  
 266 Choudhary and Krishnan, 2011, Kumar et al., 2017). The contribution of convective rainfall to the total rainfall appears to be  
 267 more than 80 % in GFS T1534 forecasts for all lead times (Fig. 7c). ~~A~~ ~~S~~ similar overestimation of convective rainfall in GFS  
 268 T1534 is reported by Ganai et al. (2021). The observed convective (large-scale) rainfall ratio is around 55 % (45 %) as  
 269 shown in Abhik et al. (2017). The HGFM forecast shows relative improvement in predicting convective and large-scale  
 270 rainfall ratios compared to GFS T1534 (Fig. 7c and 7d). The decrease (increase) in convective (large-scale) rainfall  
 271 contribution to total rain is noted in HGFM forecast. The finer horizontal resolution in HGFM possibly allows for a more  
 272 accurate representation of deep convection due to scale-aware representation.



273



274

275

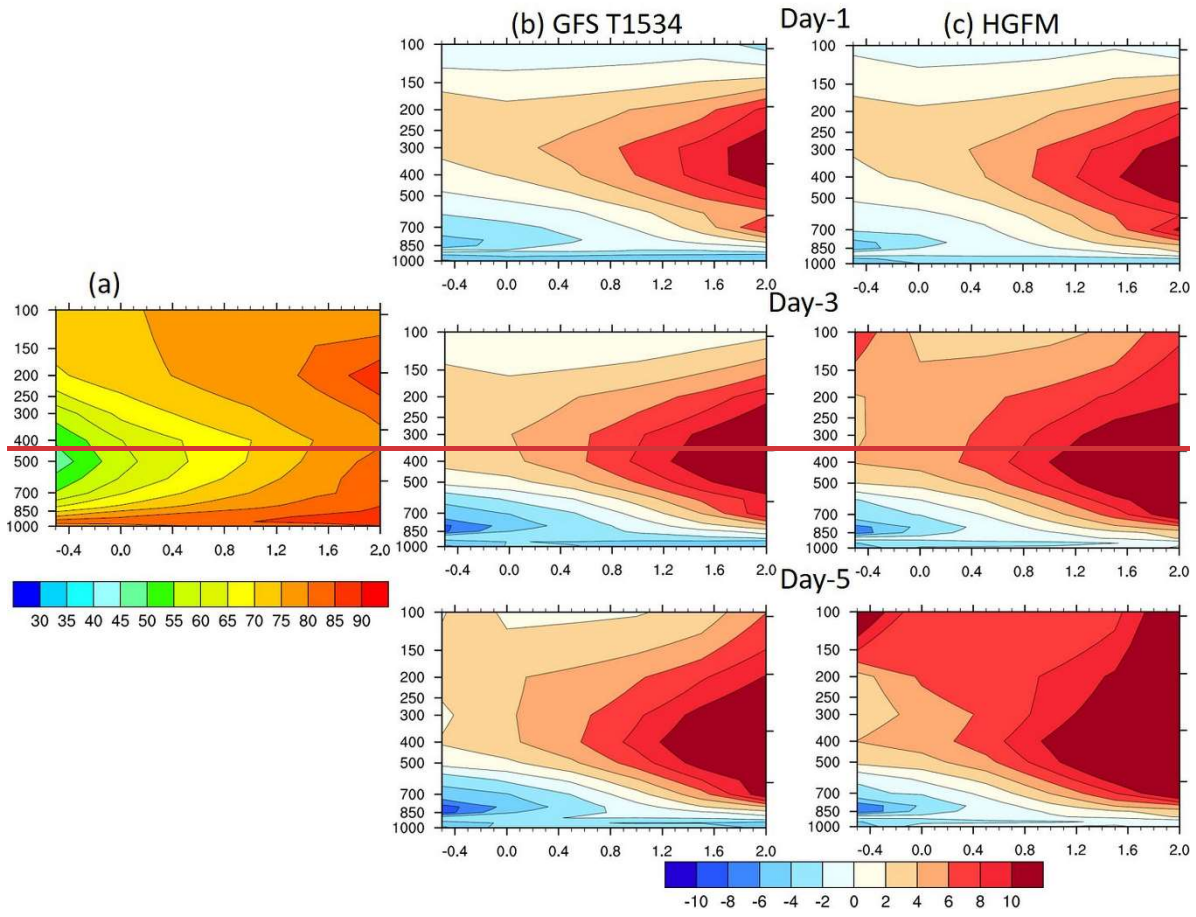
276 **Figure 7. Comparison of easterly shear (m/s) from ERA-5 with GFS T1534 (a) and HGFM (b) along with convective/total rainfall**  
 277 **(c) and large scale/total rainfall (d) between GFS T1534 and HGFM during JJAS 2022 for day-1 day-3 and day-5 lead time.**

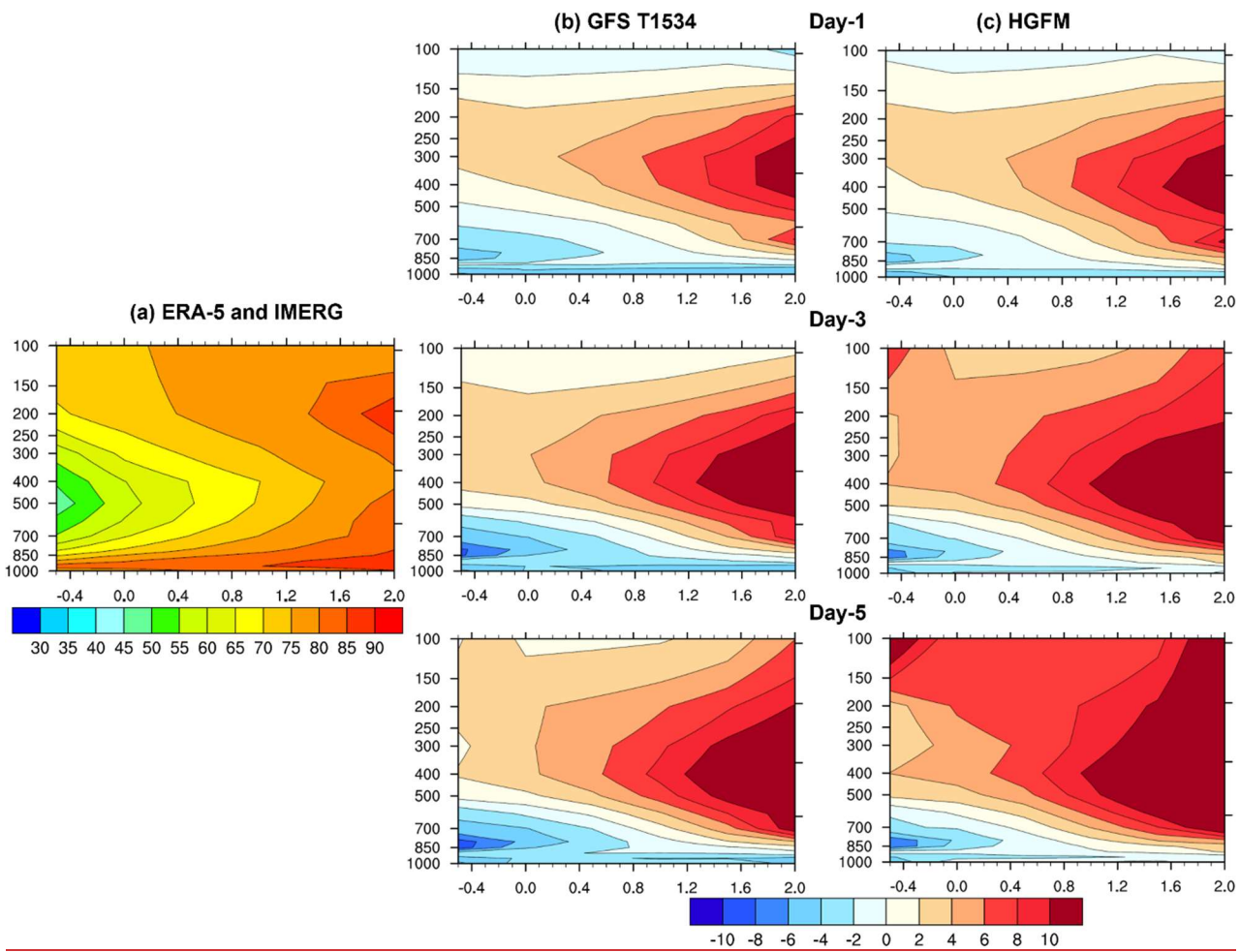
278 To attain further clarity about the model precipitation and moist convective processes, the vertical profile of relative  
 279 humidity as a function of rain rate is analyzed for JJAS of 2022 over the ISM region (60° E-100° E, 10° S-30° N). The bias  
 280 analysis suggests that GFS T1534 has systematically underestimated the lower-level moisture for all lead times (Fig. 8b).

281 ~~This It~~ is consistent with the ~~study by findings of~~ Mukhopadhyay et al. (2019), and Ganai et al. (2021), ~~who where they~~  
 282 reported ~~a~~ similar underestimation of lower-level moisture over the ISM region in GFS T1534 forecast. In contrast, the  
 283 HGFM shows relative improvement in the lower-level moisture distribution, as depicted in Fig. 4c for all lead times. The  
 284 enhancement of the lower-level moisture is ~~visiblenoticeable-as~~ compared to ~~the~~ GFS T1534 forecast. However, the upper  
 285 troposphere is too moist for both model forecasts and ~~needrequires~~ further improvement.

286 It is observed that ~~the~~ overall statistics of monsoon rainfall and related convective processes have significantly improved in  
 287 the HGFM model. In the next section, a case of heavy rainfall is discussed, followed by the analysis of recent tropical  
 288 cyclone forecasts.

289





291

292 **Figure 8. Comparison of Relative humidity (% bias in shaded) vs rain rate (mm/day) over ISM region (60° E-100° E, 10° S-30° N)**  
 293 **during JJAS-2022 from ERA-5 and IMERG (a) with GFS T1534 (b) and HGFM (c) during JJAS 2022 for day-1 day-3 and day-5**  
 294 **lead time.**

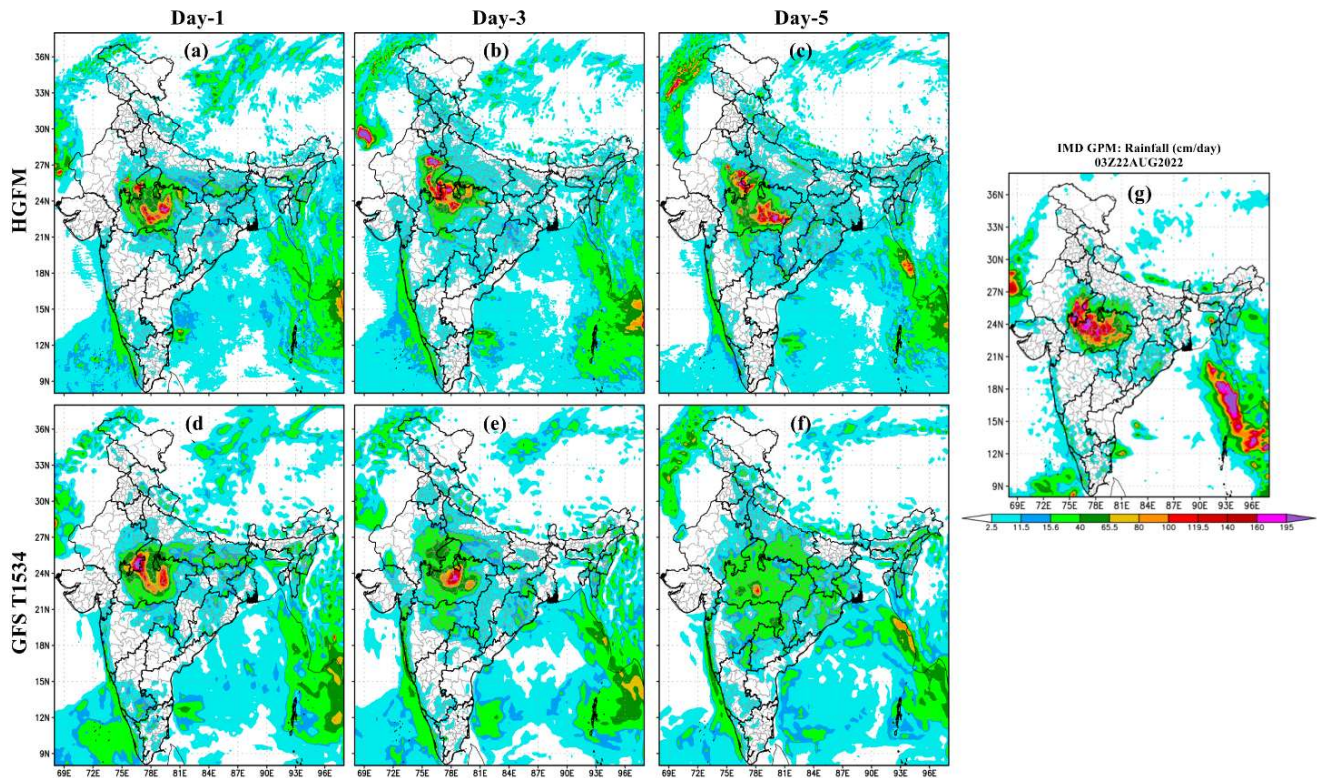
### 295 3.5 Evaluation of Heavy Rainfall event

296 A very heavy rainfall event occurred on 22 August 2022 over central India. This event was well captured by both GFS  
 297 T1534 and HGFM models as compared to the observed rain from IMD-GPM (shown in Fig. 9). Both HGFM (Fig. 9a, b, c)  
 298 and GFS T1534 (Fig. 9d, e, f) models simulated the heavy rainfall signature compared to IMD-GPM (Fig. 9g) on day 1 and  
 299 day 3 forecasts. However, a major-significant difference was noted for in rainfall intensity and spatial distribution on at longer  
 300 lead times (day 5) in HGFM and GFS T1534. There is an underestimation of rainfall in bBoth the models underestimated  
 301 rainfall compared to observations. Nevertheless, Whereas the HGFM captures the signal of the occurrence of heavy rainfall  
 302 occurrence even at day 5 lead time, which is almost negligible in the GFS T1534 forecast. Further, the precipitation  
 303 probability distribution function (PDF) is analyzed (figure not shown) for the JJAS 2022 monsoon. It is found that the



304 HGFM shows a better PDF in the very heavy (11.56-20.45 cm/day) and extreme (>20.45 cm/day) rainfall categories as  
305 compared to GFS T1534.

306



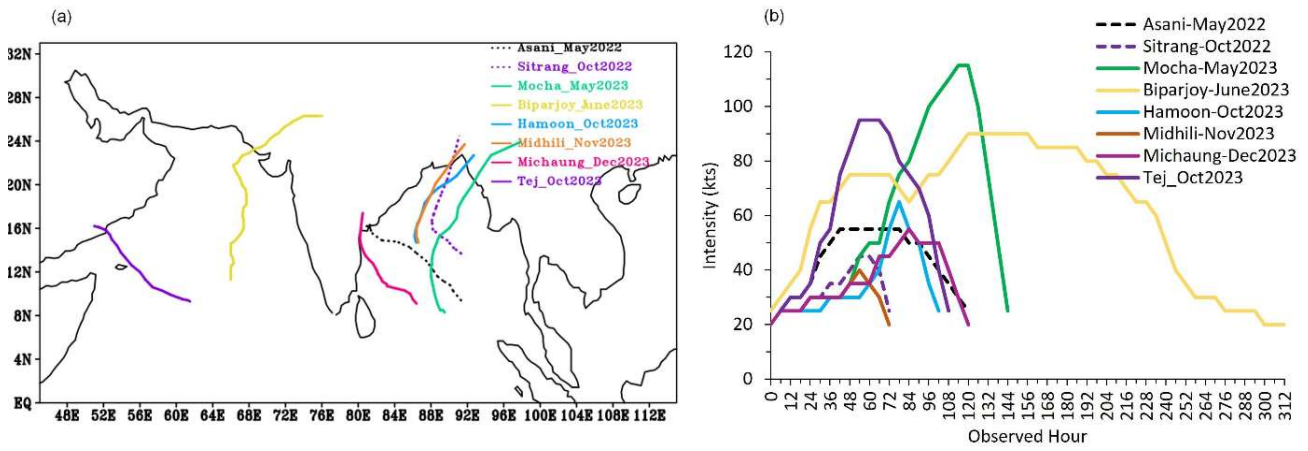
307

308 Figure 9. Comparison of heavy rainfall event on 22 August 2022 with HGFM (a, b, c), GFS T1534 (d, e, f) for day-1, day-3, and  
309 day-5 lead times with IMD GPM (g) rainfall.

### 310 3.5 Evaluation of Tropical Cyclone Forecast

311 A Total of eight named cases of tropical cyclones occurred during 2022 and 2023 (RSMC 2022, RSMC 2023), which are  
312 considered in the present study. Out of these eight cases, two cyclones formed over the Arabian Sea and six cyclones  
313 over the Bay of Bengal (BOB). The best track data of track, intensity, and landfall is obtained from IMD and referred to as  
314 observations henceforth in the text. Figure 10 shows the observed tracks (Fig. 10a) and observed intensity in terms of the  
315 Maximum Sustained Wind Speed (MSW Fig. 10b) of the cyclones. The cyclones in the present study have different tracks  
316 and various ranges of severity in terms of intensity over both the basins.

317



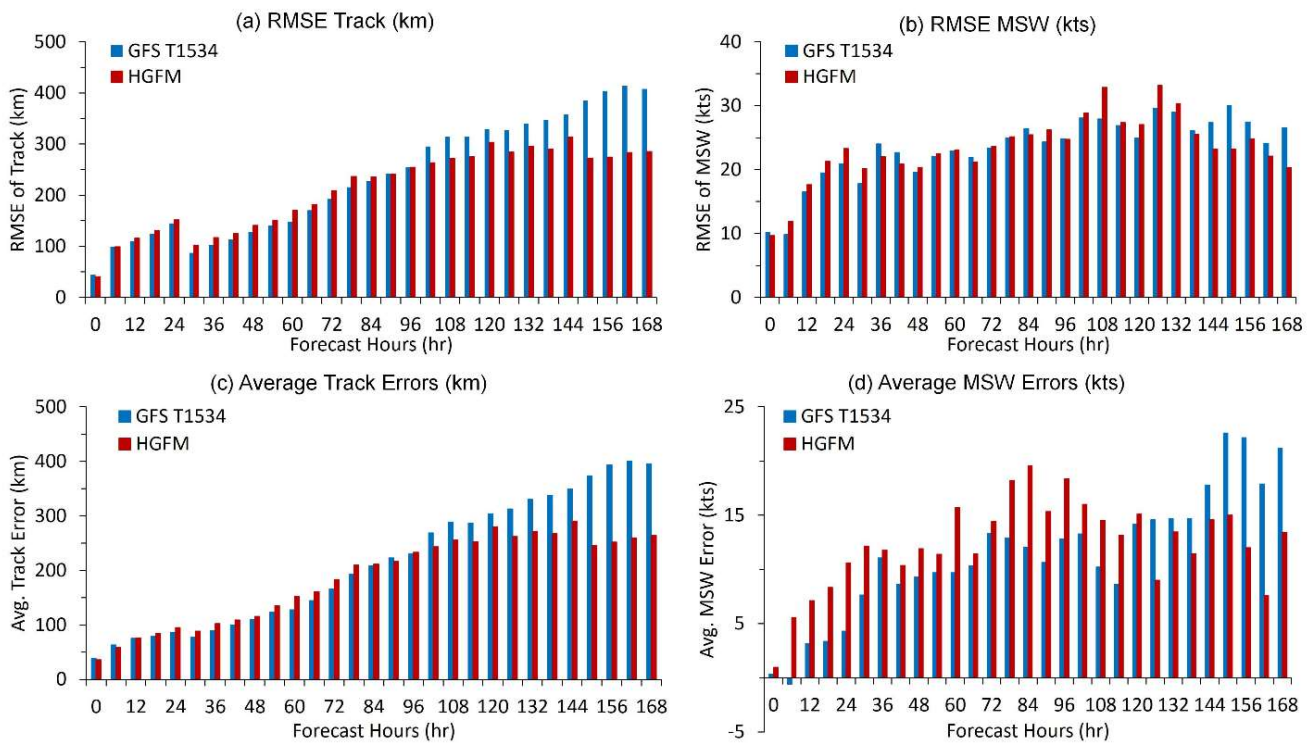
318

319 **Figure 10. a) Observed tracks of the cyclones b) Observed Intensity in terms of Maximum Sustained Wind Speed (kts) during year**  
 320 **2022-2023.**

321 **3.5.1 Verification of GFS T1534 and HGFM Forecast for tropical cyclone cases during 2022 and 2023**

322 For this verification, the lifetime of the cyclone is considered starting from the depression stage untill landfall, as per the  
 323 observation. The total sample includes; a minimum of four and a maximum 10ten initial conditions for typical cases,  
 324 depending on the life-span of the case. The errors calculated here are averaged for each forecast hour within the sample.  
 325 The Root Mean Square Error (RMSE) for track and intensity is shown in Fig. 11a and b, respectively. Initially, upto 4 days,  
 326 GFS T1534 and HGFM performs equally well, but the-considerable improvement with HGFM is noted after 4 days in both  
 327 track and intensity forecast. Figure 11c-d depicts the average track error and average intensity errors for all the cyclones.  
 328 The average track errors, as well as average intensity errors, are reduced drastically in HGFM with longer lead hours (4 days  
 329 or more). Average track errors (average intensity errors) are ~300 km (~20 kts) with 7 days leads in HGFM. The average  
 330 landfall errors (both position and time) are also evaluated with IMD observations and are shown in Fig. 12. With 4 days lead,  
 331 average landfall position errors are ~200 km in HGFM and about 250 km for GFS T1534. Overall, the landfall position  
 332 errors are less for HGFM. Remarkable improvements are seen in the average landfall time errors in HGFM throughout the  
 333 life cycle of cyclones. Overall, the track and intensity forecast are improved with HGFM for longer lead hours (~4 days or  
 334 more), which is an added advantage for the early warning and mitigation purposes. Here, one of the cyclone cases (cyclone  
 335 Biparjoy) is discussed in detail.

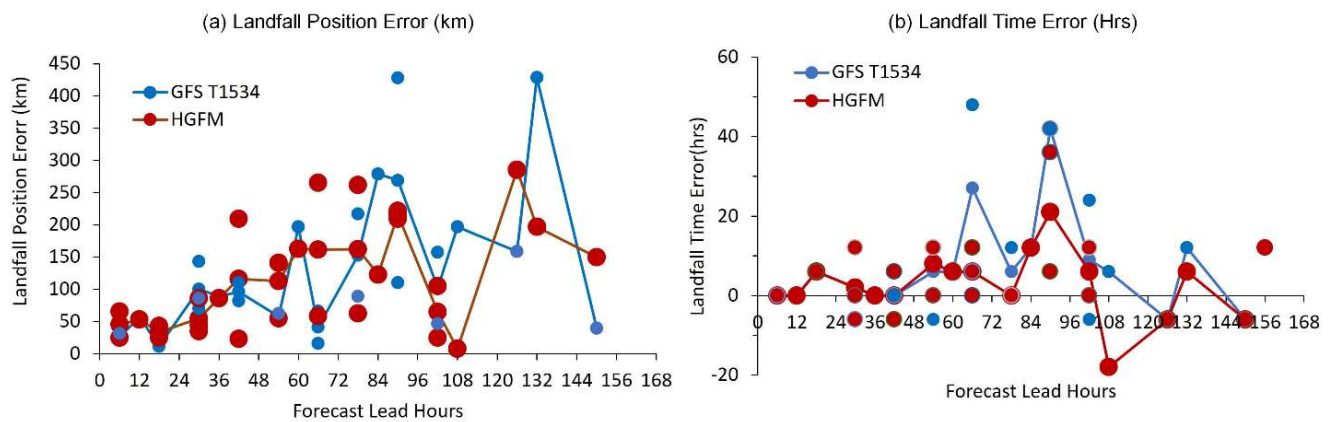
336



337

338 **Figure 11. a) RMSE of Track in km b) RMSE of MSW in kts c) Average Track error (km) d) Average Intensity Errors (kts).**

339



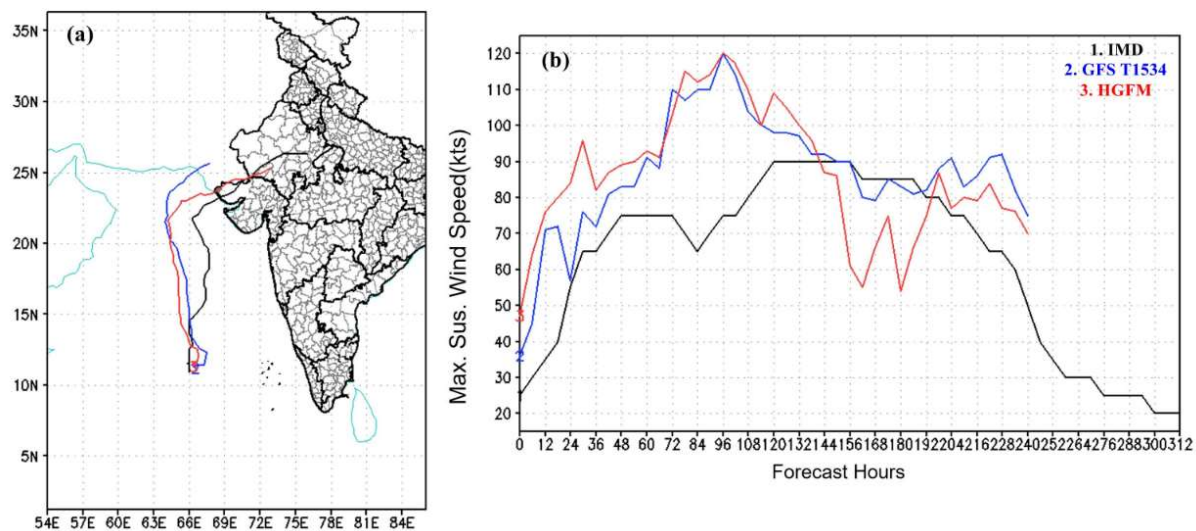
340

341 **Figure 12. a) Average Landfall position errors in km b) Average Landfall time Errors in hours. The continuous lines represent the**  
 342 **average errors for GFS T1534 (Blue) and HGFM (Red). The different sizes of the dots isare for making the overlapped points**  
 343 **visible.**

### 344 3.5.2 A case study - Cyclone Biparjoy

345 During the monsoon onset of the 2023 season, tropical cyclone Biparjoy evolved in the Arabian Sea and hit the north-  
346 western state of Gujarat, India. The cyclone Biparjoy lasted for quite a long-time during 6-19 June 2023. As seen in figure  
347 13a, it moved almost parallel to the Indian west coast and ~~had aeventually~~ recurred to ~~finally~~ make landfall over the northern  
348 part of Gujarat and adjoining Pakistan. It ~~underwentpassed through the~~ rapid intensification during its genesis and growthing  
349 stages on 6 and 7 June. ~~This case was particularly challenging for prediction due to combination of recurving track, rapid~~  
350 intensification, slow movement, and a long lifespan. The HGFM and GFS T1534 track, and intensity forecast of TC  
351 Biparjoy, based on 6 June (day of genesis) initial condition, ~~isare~~ shown in Fig. 13 a and b, along with the best track data  
352 from IMD. It is evident that the HGFM predicts a track much closer to the observation compared to GFS T1534.  
353 Particularly, the recurvature is better captured by HGFM at about 6-7 days lead time. Both ~~the~~ models overestimated the  
354 intensity untill 120 hrs of forecast, ~~and thereafter~~ which they ~~indicatesd~~ the dissipation phase.

355



356

357

358 **Figure 13. (a) track and (b) intensity variation forecast by GFS T1534, HGFM and as reported by IMD for the case of**  
359 **oTropical cyclone Biparjoy over Arabian Sea based on 6 June 2023 initial condition.**

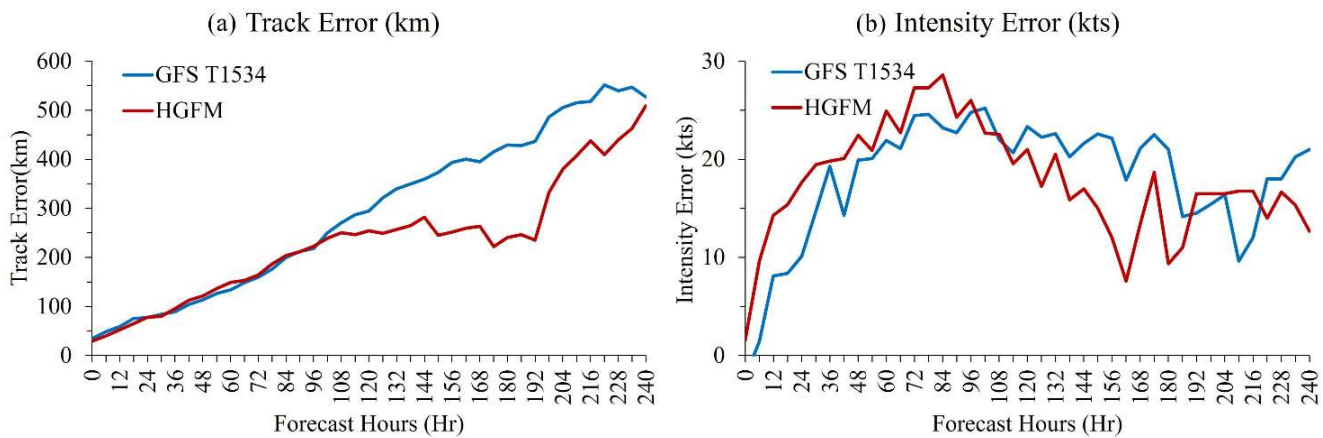
360 To ~~assessknew~~ the robustness of the performance, ~~the~~ verification is carried out for this particular case considering forecasts  
361 from all the initial conditions (from 6 June 00UTC to 15 June 00UTC, initialized at 24 ~~hours~~ interval). A comparative  
362 analysis of landfall position and landfall time errors ~~forwith~~ HGFM and GFS T1534, with respect to ~~the data that~~ reported by  
363 IMD, ~~is presented has been mentioned~~ in Table 2. It is evident that the landfall position error of the cyclone has been

364 significantly improved by HGFM forecast, though the landfall time error appears to be almost equivalent as compared to  
 365 GFS T1534. Further, the average track and intensity errors (obtained from a total of 10 initial conditions) isare depicted in  
 366 Fig. 14a and 14b. It is evident that ~~the~~ HGFM ~~produces~~ consistently produces accurate predictions of track and intensity with  
 367 lesser errors ~~on~~at longer lead times, while the errors for shorter lead times are more or less the same ~~for shorter lead~~.

369 **Table 2. Landfall position (km) and landfall time (hr) errors for the forecasts started with different initial conditions. -ve (+ve )**  
 370 **sign indicates early (late) landfall with respect to observed landfall time. The bold numbers indicates the significant improvement**  
 371 **in the landfall position errors with HGFM.**

Forecast Hours from Observed landfall (Hr)	Initial Condition	Landfall Position Error (km)		Landfall Time Error (Hr)		372
		GFS T1534	HGFM	GFS T1534	HGFM	373
228	2023060600	298	<b>57</b>	0	-30	374
204	2023060700	No Landfall				375
180	2023060800	616	<b>201</b>	0	0	376
156	2023060900	349	<b>197</b>	12	12	377
132	2023061000	428	<b>197</b>	12	6	378
108	2023061100	197	<b>7</b>	6	-18	379
84	2023061200	279	<b>123</b>	12	12	380
60	2023061300	197	<b>163</b>	6	6	381
36	2023061400	89	<b>86</b>	0	0	382
12	2023061500	57	<b>53</b>	0	0	383
						384
						385
						386
						387
						388
						389
						390

391



392  
 393 **Figure 14. a) Average track error and b) average intensity error for the tropical cyclone Biparjoy over Arabian Sea.**

394 **4 Conclusions**

395 For the first time, a version of the GFS model utilizing a new grid structure, the triangular cubic octahedral (Tco) grid, has  
 396 been developed and is being run on an experimental basis for short to medium-range weather prediction over the Indian  
 397 region, designated as IITM High resolution Global Forecast Model (HGFM). The Tco grid provides a higher resolution over  
 398 the tropics, enablingmaking the model to achieve a 6.5 km horizontal resolution near the tropics. This higher resolution  
 399 represents a substantial leap from the existing Gaussian linear GFS T1534 which maintains a resolution of 12.5 km across  
 400 the globe. The KE spectra of 200 hPa zonal wind have also revealed reasonable power by both the models with HGFM  
 401 showing marginally better power in the Kolmogorov region, indicating the fidelity of the model structure.

402 It is worth to-mentioning that the present dynamical core, using the cubic octahedral grid, has been-is implemented in  
 403 ECMWF weather forecast model since 2016 (Malardel et al., 2016). This has led to a significant increase in forecast  
 404 accuracy and computational efficiency in the ECMWF model. In the present study, it is found that the-above-this dynamical  
 405 core in the GFS T1534 has improved the orographic rainfall and reduces the Gibbs noise over the mountainous regions, in  
 406 addition to improved precipitation skill over the Indian landmass region. The June-September monsoon rainfall and a case  
 407 study of heavy rainfall have been analyzed in detail. The newly developed HGFM shows significantly better skill,  
 408 particularly in the longer lead and for heavier rain categories. Rainfall biases over the wholeentire globe appear to-be broadly  
 409 similar between HGFM and GFS T1534. A case of heavy~~yer~~ rainfall in and around central India during the monsoon season  
 410 has been analysed, where the-validation shows a significant gain in forecast lead time by the-HGFM compared to GFS  
 411 T1534. The HGFM captures the rainfall signature at 5 days lead time, when there is hardly any indication in the HGFM-GFS  
 412 T1534 model forecast.

413 Several cases of tropical cyclones during 2022 and 2023 were analysed, indicating better performance of HGFM compared  
 414 to GFS T1534 in predicting tracks and intensity. A detailed evaluation case-of tropical cyclone Biparjoy, has-been-evaluated

415 ~~in detail~~ based on IMD observation, ~~revealsIt is seen~~ that the HGFM model ~~providesgenerates~~ better accuracy ~~ofin~~ cyclone  
416 position ~~inacross~~ -almost all lead times (Table 2). ~~and further~~Additionally, the average track error ~~for HGFM is significantly~~  
417 ~~lower than also is found to be much lesser as compared to~~GFS T1534 ~~inat~~ longer lead ~~times~~. However, the ~~errors of both~~  
418 ~~model in~~average track and intensity ~~errors for both the models~~ are found to be equivalent. This paper highlights the initial  
419 results of the newly developed HGFM model and its skill as compared to the operational GFS T1534 model. Subsequently  
420 more analyses for many events will be carried out and the model will be made operational for weather forecasts over India.  
421 The current set-up of the HGFM model uses the same physics as the GFS model. However, the HGFM model would require  
422 some parameter tuning to optimize ~~and enhance~~ the performance of the model and ~~increase~~its fidelity. The future work will  
423 be focused on detailed validation of model simulations with optimal set of physical parameterizations.

424

425

426

427

428

429

#### 430 **Code and Data Availability**

431 The model simulated data used for HGFM and GFS T1534 in the study are available at “TCO model data” by R Phani  
432 Murali Krishna, Kumar Siddharth, Athipatta Gopinathan Prajeesh, Malay Ganai, B. Revanth Reddy, Kumar Roy and  
433 Parthasarathi Mukhopadhyay, DOI: <https://doi.org/10.5281/zenodo.12569807>. The model code is available at "GFS TCO  
434 Model code" by R Phani Murali Krishna, Kumar Siddharth, Athipatta Gopinathan Prajeesh, Parthasarathi Mukhopadhyay.  
435 DOI: <https://doi.org/10.5281/zenodo.12526400>

436

#### 437 **Author Contributions**

438 RPMK, SK, AGP and PM conceptualised the problem and made necessary changes/modification development of code for  
439 Tco and wrote the major part of the Introduction, data, methodology and over all sequences. PB and NW helped during  
440 formulation of the Tco grid in GFS and helped in improving the manuscript writing. KR, MG, ST, BRR and TG made all the  
441 forecast analysis of monsoon parameters and wrote the respective portion on analyses. RK, MD and SS made the analysis  
442 related to cyclone forecast by HGFM model and wrote the section on the cyclone forecast analysis and BRR made the  
443 dCAPE analysis and extracted the post processed variables for the analysis.

444

445

446 **Competing interests**

447 The authors declare that they have no conflict of interest.

448

449

450 **Disclaimer**

451

452

453

454 **Acknowledgments**

455 IITM is fully funded by the Ministry of Earth Sciences, Government of India. We would like to thank ECMWF for their  
456 support during the model development and for providing the ERA5 data set. We thank NCMRWF for providing the GFS  
457 initial conditions used for conducting simulations. We acknowledge Pratyush High Performance Computing at IITM, Pune  
458 for providing the computing facility to carry out the simulations. We thank Mr. Vaishak for helping in archiving the data in  
459 ARDC server. Authors thank Secretary Ministry of Earth Sciences, Government of India and Director, IITM for support and  
460 facilities provided for this study. We thank IMD for providing the IMD-GPM rainfall and cyclone best track data.

461

462

463

464

465

466

467

468

469

470

471



472 **References**

- 473 Abhik, S., Halder, M., Mukhopadhyay, P., Jiang, X., and Goswami, B.N.: A possible new mechanism for northward  
474 propagation of boreal summer intraseasonal oscillations based on TRMM and MERRA reanalysis, *Clim. Dyn.*, 40, 1611-  
475 1624, <https://doi.org/10.1007/s00382-012-1425-x>, 2013.
- 476 Abhik, S., Krishna, R.P.M., Mahakur, M., Ganai, M., Mukhopadhyay, P., and Dudhia, J.: Revised cloud processes to  
477 improve the mean and intraseasonal variability of Indian summer monsoon in climate forecast system: Part 1, *J. Adv.*  
478 *Model. Earth. Syst.*, 9(2), 1002-1029, <https://doi.org/10.1002/2016MS000819>, 2017.
- 479 Alpert, J.C., Kanamitsu, M., Caplan, P.M., Sela, J.G., White, G.H., and Kalnay, E.: Mountain induced gravity wave drag  
480 parameterization in the NMC medium-range forecast model. In Conference on Numerical Weather Prediction, Baltimore,  
481 MD, 8<sup>th</sup>, 726-733, 1988.
- 482 Arakawa, A. and Schubert, W.H.: Interaction of a cumulus cloud ensemble with the large-scale environment, Part I, *J.*  
483 *Atmos. Sci.*, 31(3), 674-701, [https://doi.org/10.1175/1520-0469\(1974\)031<0674:IOACCE>2.0.CO;2](https://doi.org/10.1175/1520-0469(1974)031<0674:IOACCE>2.0.CO;2), 1974.
- 484 Arakawa, A. and Wu, C.M.: A unified representation of deep moist convection in numerical modeling of the atmosphere.  
485 Part I, *J. Atmos. Sci.*, 70(7), 1977-1992, <https://doi.org/10.1175/JAS-D-12-0330.1>, 2013.
- 486 Bechtold, P., Köhler, M., Jung, T., Doblas-Reyes, F., Leutbecher, M., Rodwell, M. J., Vitart, F., and Balsamo, G.: Advances  
487 in simulating atmospheric variability with the ECMWF model: From synoptic to decadal time-scales, *Q. J. Roy. Meteor.*  
488 *Soc.*, 134, 1337–1351, <https://doi.org/10.1002/qj.289>, 2008.
- 489 Chattopadhyay, R., Goswami, B.N., Sahai, A.K., and Fraedrich, K.: Role of stratiform rainfall in modifying the northward  
490 propagation of monsoon intraseasonal oscillation, *J. Geophys. Res. Atmos.*, 114(D19),  
491 <https://doi.org/10.1029/2009JD011869>, 2009.
- 492 Choudhury, A.D. and Krishnan, R.: Dynamical response of the South Asian monsoon trough to latent heating from  
493 stratiform and convective precipitation, *J. Atmos. Sci.*, 68(6), 1347-1363, <https://doi.org/10.1175/2011JAS3705.1>, 2011.
- 494 Chun, H.Y. and Baik, J.J.: Momentum flux by thermally induced internal gravity waves and its approximation for large-scale  
495 models, *J. Atmos. Sci.*, 55(21), 3299-3310, [https://doi.org/10.1175/1520-0469\(1998\)055<3299:MFBTII>2.0.CO;2](https://doi.org/10.1175/1520-0469(1998)055<3299:MFBTII>2.0.CO;2), 1998.
- 496 Clough, S.A., Shephard, M.W., Mlawer, E.J., Delamere, J.S., Iacono, M.J., Cady-Pereira, K., Boukabara, S., and Brown,  
497 P.D.: Atmospheric radiative transfer modeling: A summary of the AER codes, *J. Quant. Spectrosc. Radiat. Transf.*, 91(2),  
498 233-244, <https://doi.org/10.1016/j.jqsrt.2004.05.058>, 2005.

499 Crueger, T., Giorgetta, M.A., Brokopf, R., Esch, M., Fiedler, S., Hohenegger, C., Kornblueh, L., Mauritsen, T., Nam, C.,  
500 Naumann, A.K., and Peters, K.: ICON-A, the atmosphere component of the ICON earth system model: II. Model evaluation,  
501 *J. Adv. Model. Earth. Syst.*, 10(7), 1638-1662, <https://doi.org/10.1029/2017MS001233>, 2018.

502 Deng, Q., Khouider, B., and Majda, A.J.: The MJO in a coarse-resolution GCM with a stochastic multcloud  
503 parameterization, *J. Atmos. Sci.*, 72(1), 55-74. <https://doi.org/10.1175/JAS-D-14-0120.1>, 2015.

504 Deshpande, M., Kanase, R., Krishna, R.P.M., Tirkey, S., Mukhopadhyay, P., Prasad, V.S., Johny, C.J., Durai, V.R., Devi, S.  
505 and Mohapatra, M.: Global Ensemble Forecast System (GEFS T1534) evaluation for tropical cyclone prediction over the  
506 North Indian Ocean, *Mausam.*, 72(1), 119-128, <https://doi.org/10.54302/mausam.v72i1.123>, 2021.

507 ECMWF IFS DOCUMENTATION—Cy43r1 Operational Implementation Part IV: Physical Processes; ECMWF: Reading,  
508 UK, 2016.

509 Fu, X. and Wang, B.: The boreal-summer intraseasonal oscillations simulated in a hybrid coupled atmosphere–ocean  
510 model, *Mon. Weather. Rev.*, 132(11), 2628-2649, <https://doi.org/10.1175/MWR2811.1>, 2004.

511 Gadgil, S. and Gadgil, S.: The Indian monsoon, GDP and agriculture, *Econ. polit. Wkly.*, 4887-4895,  
512 <https://www.jstor.org/stable/4418949>, 2006.

513 Ganai, M., Tirkey, S., Krishna, R.P.M., and Mukhopadhyay, P.: The impact of modified rate of precipitation conversion  
514 parameter in the convective parameterization scheme of operational weather forecast model (GFS T1534) over Indian  
515 summer monsoon region, *Atmos. Res.*, 248, 105185, <https://doi.org/10.1016/j.atmosres.2020.105185>, 2021.

516 Giorgetta, M.A., Brokopf, R., Crueger, T., Esch, M., Fiedler, S., Helmert, J., Hohenegger, C., Kornblueh, L., Köhler, M.,  
517 Manzini, E., and Mauritsen, T.: ICON-A, the atmosphere component of the ICON earth system model: I. Model description,  
518 *J. Adv. Model. Earth. Syst.*, 10(7), 1613-1637, <https://doi.org/10.1029/2017MS001242>, 2018.

519 Han, J. and Pan, H.L.: Revision of convection and vertical diffusion schemes in the NCEP Global Forecast System, *Weather.*  
520 *Forecast.*, 26(4), 520-533, <https://doi.org/10.1175/WAF-D-10-05038.1>, 2011.

521 Han, J., Witek, M.L., Teixeira, J., Sun, R., Pan, H.L., Fletcher, J.K., and Bretherton, C.S.: Implementation in the NCEP GFS  
522 of a hybrid eddy-diffusivity mass-flux (EDMF) boundary layer parameterization with dissipative heating and modified stable  
523 boundary layer mixing, *Weather. Forecast.*, 31(1), 341-352, <https://doi.org/10.1175/WAF-D-15-0053.1>, 2016.

524 Han, J., Wang, W., Kwon, Y.C., Hong, S.Y., Tallapragada, V., and Yang, F.: Updates in the NCEP GFS cumulus convection  
525 schemes with scale and aerosol awareness, *Weather. Forecast.*, 32(5), 2005-2017, <https://doi.org/10.1175/WAF-D-17->  
526 0046.1, 2017.

527 Held, I.M. and Suarez, M.J.: A proposal for the intercomparison of the dynamical cores of atmospheric general circulation  
528 models, *Bull. Am. Meteorol. Soc.*, 75(10), 1825-1830, <https://doi.org/10.1175/1520->  
529 0477(1994)075<1825:APFTIO>2.0.CO;2, 1994.

530 Hersbach, H. and Dee, D.: ERA5 reanalysis is in production. ECMWF Newsletter No. 147,  
531 ECMWF, Reading, United Kingdom, 7, <http://www.ecmwf.int/sites/default/files/elibrary/2016/16299-newsletter-no147-spring->  
532 2016.pdf, 2016.

533 Hoffman, R.N., Kumar, V.K., Boukabara, S.A., Ide, K., Yang, F., and Atlas, R.: Progress in forecast skill at three leading  
534 global operational NWP centers during 2015–17 as seen in summary assessment metrics (SAMs), *Weather. Forecast.*, 33(6),  
535 1661-1679, <https://doi.org/10.1175/WAF-D-18-0117.1>, 2018.

536 Huffman, G.J., Stocker, E.F., Bolvin, D.T., Nelkin, E.J., and Tan, J.: GPM IMERG Final Precipitation L3 Half Hourly 0.1  
537 degree x 0.1 degree V06, Greenbelt, MD, Goddard Earth Sciences Data and Information Services Center (GES DISC),  
538 Accessed: 20 March 2023, doi:10.5067/GPM/IMERG/3B-HH/06, 2019.

539 Iacono, M.J., Mlawer, E.J., Clough, S.A., and Morcrette, J.J.: Impact of an improved longwave radiation model, RRTM, on  
540 the energy budget and thermodynamic properties of the NCAR community climate model, CCM3, *J. Geophys. Res. Atmos.*,  
541 105(D11), 14873-14890, <https://doi.org/10.1029/2000JD900091>, 2000.

542 Jiang, X., Li, T., and Wang, B.: Structures and mechanisms of the northward propagating boreal summer intraseasonal  
543 oscillation, *J. Clim.*, 17(5), 1022-1039, [https://doi.org/10.1175/1520-0442\(2004\)017<1022:SAMOTN>2.0.CO;2](https://doi.org/10.1175/1520-0442(2004)017<1022:SAMOTN>2.0.CO;2), 2004.

544 Kanase, R., Tirkey, S., Deshpande, M., Krishna, R.P.M., Johny, C.J., Mukhopadhyay, P., Iyengar, G., and Mohapatra, M.:  
545 Evaluation of the Global Ensemble Forecast System (GEFS T1534) for the probabilistic prediction of cyclonic disturbances  
546 over the North Indian Ocean during 2020 and 2021, *J. Earth. Sys. Sci.*, 132-143, <https://doi.org/10.1007/s12040-023-02166->  
547 2, 2023.

548 Kim, Y.J. and Arakawa, A.: Improvement of orographic gravity wave parameterization using a mesoscale gravity wave  
549 model, *J. Atmos. Sci.*, 52(11), 1875-1902, [https://doi.org/10.1175/1520-0469\(1995\)052<1875:IOOGWP>2.0.CO;2](https://doi.org/10.1175/1520-0469(1995)052<1875:IOOGWP>2.0.CO;2), 1995.

550 Kinter, J. L., III, Cash, B., Achuthavarier, D., Adams, J., Altshuler, E., Dirmeyer, P., Doty, B., Huang, B., Jin, E. K., Marx,  
551 L., Manganello, J., Stan, C., Wakefield, T., Palmer, T., Hamrud, M., Jung, T., Miller, M., Towers, P., Wedi, N., Satoh, M.,  
552 Tomita, H., Kodama, C., Nasuno, T., Oouchi, K., Yamada, Y., Taniguchi, H., Andrews, P., Baer, T., Ezell, M., Halloy, C.,  
553 John, D., Loftis, B., Mohr, R., & Wong, K.: Revolutionizing Climate Modeling with Project Athena: A Multi-Institutional,  
554 International Collaboration. *Bull. Am. Meteorol. Soc.*, 94(2), 231-245. <https://doi.org/10.1175/BAMS-D-11-00043.1>, 2013.

555 Kumar, S., Arora, A., Chattopadhyay, R., Hazra, A., Rao, S.A., and Goswami, B.N.: Seminal role of stratiform clouds in  
556 large-scale aggregation of tropical rain in boreal summer monsoon intraseasonal oscillations, *Clim. Dyn.*, 48, 999-1015,  
557 <https://doi.org/10.1007/s00382-016-3124-5>, 2017.

558 Kumar, S., Phani, R., Mukhopadhyay, P., and Balaji, C.: Does increasing horizontal resolution improve seasonal prediction  
559 of Indian summer monsoon?: A climate forecast system model perspective, *Geophys. Res. Lett.*, 49(7), e2021GL097466,  
560 <https://doi.org/10.1029/2021GL097466>, 2022.

561 Li, J., Yu, R., Yuan, W., Chen, H., Sun, W. and Zhang, Y.: Precipitation over East Asia simulated by NCAR CAM5 at  
562 different horizontal resolutions. *J. Adv. Model. Earth. Syst.*, 7(2), 774-790, <https://doi.org/10.1002.2014MS000414>,  
563 2015. Lott, F. and Miller, M.J.: A new subgrid-scale orographic drag parametrization: Its formulation and testing, *Q. J. R.*  
564 *Meteorol. Soc.*, 123(537), 101-127, <https://doi.org/10.1002/qj.49712353704>, 1997.

565 Magnusson, L. and Källén, E.: Factors influencing skill improvements in the ECMWF forecasting system, *Mon. Weather.*  
566 *Rev.*, 141(9), 3142-3153, <https://doi.org/10.1175/MWR-D-12-00318.1>, 2013.

567 Majewski, D., Liermann, D., Prohl, P., Ritter, B., Buchhold, M., Hanisch, T., Paul, G., Wergen, W. and Baumgardner, J.:  
568 The operational global icosahedral-hexagonal gridpoint model GME: description and high resolution tests, *Mon. Wea. Rev.*,  
569 130, 319– 338, [https://doi.org/10.1175/1520-0493\(2002\)130<0319:TOGIHG>2.0.CO;2](https://doi.org/10.1175/1520-0493(2002)130<0319:TOGIHG>2.0.CO;2), 2002.

570 Malardel, S., N, Wedi., W, Deconinck., M, Diamantakis., C, Kühnlein., G, Mozdzyński., M, Hamrud. and P,  
571 Smolarkiewicz.: A new grid for the IFS, ECMWF Newsletter No. 146, 23–28, 2016.

572 Mitra, A.K., Prakesh, S., Imranali, M.M., Pai, D.S. and Srivastava, A.K.: Daily merged satellite gauge real-time rainfall  
573 dataset for Indian Region, *Vayumandal*, 40(1-4), 33-43, 2014.

574 Miura, H., Satoh, M., Nasuno, T., Noda, A. T., and Oouchi, K.: A Madden-Julian Oscillation event realistically simulated by  
575 a global cloud-resolving model, *Sci.*, 318(5857), 1763–1765, <https://doi.org/10.1126/science.1148443>, 2007.

576 Molod, A., Takacs, L., Suarez, M., and Bacmeister, J.: Development of the GEOS-5 atmospheric general circulation model:  
577 Evolution from MERRA to MERRA2, *Geosci. Model. Dev.*, 8(5), 1339-1356, <https://doi.org/10.5194/gmd-8-1339-2015>,  
578 2015.

579 Mukhopadhyay, P., Prasad, V.S., Krishna, R.P.M., Deshpande, M., Ganai, M., Tirkey, S., Sarkar, S., Goswami, T., Johny,  
580 C.J., Roy, K., and Mahakur, M.: Performance of a very high-resolution global forecast system model (GFS T1534) at 12.5  
581 km over the Indian region during the 2016–2017 monsoon seasons, *J. Earth. Sys. Sci.*, 128, 1-18,  
582 <https://doi.org/10.1007/s12040-019-1186-6>, 2019.

583 Mukhopadhyay, P., Bechtold, P., Zhu, Y., Murali Krishna, R.P., Kumar, S., Ganai, M., Tirkey, S., Goswami, T., Mahakur,  
584 M., Deshpande, M., and Prasad, V.S.: Unraveling the mechanism of extreme (more than 30 sigma) precipitation during  
585 August 2018 and 2019 over Kerala, India, *Weather. Forecast.*, 36(4), 1253-1273, <https://doi.org/10.1175/WAF-D-20-0162.1>,  
586 2021.

587 Nastrom, G.D. and Gage, K.S.: A climatology of atmospheric wavenumber spectra of wind and temperature observed by  
588 commercial aircraft, *J. Atmos. Sci.*, 42, 950–960, [https://doi.org/10.1175/1520-0469\(1985\)042<0950:ACOAWS>2.0.CO;2](https://doi.org/10.1175/1520-0469(1985)042<0950:ACOAWS>2.0.CO;2),  
589 1985.

590 Pan, H.L. and Wu, W.S.: Implementing a mass flux convection parameterization package for the NMC medium-range  
591 forecast model. <https://repository.library.noaa.gov/view/noaa/11429>, 1995.

592 Prakash, S., Mitra, A.K., Momin, I.M., Rajagopal, E.N., Milton, S.F., and Martin, G.M.: Skill of short-to medium-range  
593 monsoon rainfall forecasts from two global models over India for hydro-meteorological applications, *Meteorol. Appl.*, 23(4),  
594 574-586, <https://doi.org/10.1002/met.1579>, 2016.

595 Prasad, V.S., Mohandas, S., Gupta, M.D., Rajagopal, E.N., and Dutta, S.K.: Implementation of upgraded global forecasting  
596 systems (T382L64 and T574L64) at NCMRWF, In NCMRWF Technical Report, 1-72, 2011.

597 Prasad, V.S., Mohandas, S., Dutta, S.K., Gupta, M.D., Iyengar, G.R., Rajagopal, E.N., and Basu, S.: Improvements in  
598 medium range weather forecasting system of India, *J. Earth. Sys. Sci.*, 123, 247-258, <https://doi.org/10.1007/s12040-014-599-0404-5>, 2014.

600 Prasad, V.S., Johny, C.J., Mali, P., Singh, S.K., and Rajagopal, E.N.: Global retrospective analysis using NGFS for the  
601 period 2000–2011, *Current Sci.*, 370-377, <https://www.jstor.org/stable/24912364>, 2017.

602 Rajendran, K., Kitoh, A., Mizuta, R., Sajani, S., and Nakazawa, T.: High-resolution simulation of mean convection and its  
603 intraseasonal variability over the tropics in the MRI/JMA 20-km mesh AGCM, *J. Clim.*, 21(15), 3722-3739,  
604 <https://doi.org/10.1175/2008JCLI1950.1>, 2008.

605 Rao, S.A., Goswami, B.N., Sahai, A.K., Rajagopal, E.N., Mukhopadhyay, P., Rajeevan, M., Nayak, S., Rathore, L.S.,  
606 Sheno, S.S.C., Ramesh, K.J., and Nanjundiah, R.S.: Monsoon mission: a targeted activity to improve monsoon prediction  
607 across scales, *Bull. Am. Meteorol. Soc.*, 100(12), 2509-2532, <https://doi.org/10.1175/BAMS-D-17-0330.1>, 2019.

608 Raymond, D. J.: Convection in the east Pacific Intertropical Convergence Zone, *Geophys. Res. Lett.*, 44, 562-568,  
609 [doi:10.1002/2016GL071554](https://doi.org/10.1002/2016GL071554), 2017.

610 RSMC Report, Report on Cyclonic disturbances over North Indian Ocean during 2022, India Meteorological Department,  
611 [https://rsmcnewdelhi.imd.gov.in/report.php?internal\\_menu=Mjc=](https://rsmcnewdelhi.imd.gov.in/report.php?internal_menu=Mjc=)

612 RSMC Report, Report on Cyclonic disturbances over North Indian Ocean during 2023, India Meteorological Department,  
613 [https://rsmcnewdelhi.imd.gov.in/report.php?internal\\_menu=Mjc=](https://rsmcnewdelhi.imd.gov.in/report.php?internal_menu=Mjc=)

614 Satoh, M., Tomita, H., Miura, H., Iga, S., and Nasuno, T.: Development of a global cloud resolving model-a multi-scale  
615 structure of tropical convections, *J. Earth. Simul.*, 3, 11-19, 2005.

616 Satoh, M., Stevens, B., Judt, F., Khairoutdinov, M., Lin, S.J., Putman, W.M., and Düben, P.: Global cloud-resolving models,  
617 *Curr. Clim. Change Rep.*, 5, 172-184, <https://doi.org/10.1007/s40641-019-00131-0>, 2019.

618 Skamarock, W.C.: Evaluating Mesoscale NWP Models Using Kinetic Energy Spectra, *Mon. Weather. Rev.*, 132,3019–3032,  
619 <https://doi.org/10.1175/MWR2830.1>, 2004.

620 Skamarock, W.C., Klemp, J.B., Duda, M.G., Fowler, L.D., Park, S.H., and Ringler, T.D.: A multiscale nonhydrostatic  
621 atmospheric model using centroidal Voronoi tessellations and C-Grid staggering, *Mon. Weather. Rev.*, 140(9), 3090–  
622 3105, <https://doi.org/10.1175/MWR-D-11-00215.1>, 2012.

623 Staniforth, A. and Thuburn, J.: Horizontal grids for global weather and climate prediction models: a review. *Q. J. R.*  
624 *Meteorol. Soc.*, 138(662), 1-26, <https://doi.org/10.1002/qj.958>, 2012.

625 Stephens, G.L., L'Ecuyer, T., Forbes, R., Gettelmen, A., Golaz, J.C., Bodas-Salcedo, A., Suzuki, K., Gabriel, P., and Haynes,  
626 J.: Dreary state of precipitation in global models, *J. Geophys. Res. Atmos.*, 115(D24), <https://doi.org/10.1029/2010JD014532>,  
627 2010.

- 628 Sundqvist, H., Berge, E., and Kristjánsson, J.E.: Condensation and cloud parameterization studies with a mesoscale  
629 numerical weather prediction model, *Mon. Weather. Rev.*, 117(8), 1641-1657, [https://doi.org/10.1175/1520-0493\(1989\)117<1641:CACPSW>2.0.CO;2](https://doi.org/10.1175/1520-0493(1989)117<1641:CACPSW>2.0.CO;2), 1989.
- 631 Watson, P.A., Berner, J., Corti, S., Davini, P., von Hardenberg, J., Sanchez, C., Weisheimer, A., and Palmer, T.N.: The  
632 impact of stochastic physics on tropical rainfall variability in global climate models on daily to weekly time scales, *J.*  
633 *Geophys. Res. Atmos.*, 122(11), 5738-5762, <https://doi.org/10.1002/2016JD026386>, 2017.
- 634 Wedi, N.P., Polichtchouk, I., Dueben, P., Anantharaj, V.G., Bauer, P., Boussetta, S., Browne, P., Deconinck, W., Gaudin,  
635 W., Hadade, I., and Hatfield, S.: A baseline for global weather and climate simulations at 1 km resolution, *J. Adv. Model.*  
636 *Earth. Syst.*, 12(11), e2020MS002192, <https://doi.org/10.1029/2020MS002192>, 2020.
- 637 Westra, S., Fowler, H.J., Evans, J.P., Alexander, L.V., Berg, P., Johnson, F., Kendon, E.J., Lenderink, G., and Roberts, N.:  
638 Future changes to the intensity and frequency of short-duration extreme rainfall, *Rev. Geophys.*, 52(3), 522-555,  
639 <https://doi.10.1002/2014RG000464>, 2014.
- 640 Zhang, G.J.: Convective quasi-equilibrium in the tropical western Pacific: Comparison with midlatitude continental  
641 environment, *J. Geophys. Res. Atmos.*, 108(D19), <https://doi.org/10.1029/2003JD003520>, 2003.
- 642 Zhao, Q. and Carr, F.H.: A prognostic cloud scheme for operational NWP models, *Mon. Weather. Rev.*, 125(8), 1931-1953,  
643 [https://doi.org/10.1175/1520-0493\(1997\)125<1931:APCSFO>2.0.CO;2](https://doi.org/10.1175/1520-0493(1997)125<1931:APCSFO>2.0.CO;2), 1997.